Influence of loading path on ductile fracture of tensile specimens made from aluminium alloys

Lars Edvard Bryhni Dæhli*, Tore Børvik, Odd Sture Hopperstad

Structural Impact Laboratory (SIMLab), Centre for Research-based Innovation (CRI), Department of Structural Engineering, Norwegian University of Science and Technology, NO-7491 Trondheim, Norway

Abstract

Experimental data and numerical simulations of tensile tests on four different aluminium alloys are used to investigate the effect of loading path on ductile fracture. Micromechanical studies are undertaken by the use of axisymmetric unit cells. Stress triaxiality is extracted from the critical element in numerical simulations of smooth tensile tests and used as input in the subsequent cell simulations. The stress triaxiality evolution of the unit cell is prescribed as either i) strain-averaged values or ii) continuous functions of equivalent strain in order to examine possible effects of loading path on ductile fracture properties. Results from these simulations clearly demonstrate the importance of non-proportional loading paths on the predicted ductility of the aluminium alloys used in this investigation. The micromechanical model is finally used to estimate initial porosity values such that failure strain values from the tensile experiments are replicated in unit cell simulations. Both the conventional J_2 flow theory and the Gurson-Tvergaard porous plasticity model are used in simulations of smooth and notched tensile specimens, and the results are compared with experimental data. Simulation results for the smooth tensile specimens are in good correspondence with experiments for both descriptions of plastic flow. Simulations of notched tensile specimens with the J_2 model are shown to overestimate the tensile stress. This deficiency is not remedied by the inherent softening behaviour of the Gurson-Tvergaard model. However, the Gurson-Tvergaard model is seen to predict the ductility quite well for all the tensile specimens and aluminium alloys examined in this paper.

Keywords: Ductile fracture; Non-proportional loading; Aluminium alloys; Micromechanics; Unit cell modelling; Gurson-Tvergaard model

1. Introduction

Material ductility is often decisive for practical applications, such as energy absorbing structures, where structural components are deformed extensively leading to large plastic deformations. However, the material should not be severely damaged or fracture during these deformation processes, which must be accounted for in the design phase of such structures. Predictive descriptions of ductile failure are of utmost importance in this regard.

Ductile fracture of metal alloys has been subject to many studies over the past decades and is known to occur by nucleation, growth and coalescence of voids. The voids either pre-exist within the material (Toda et al., 2014) or nucleate at material inclusions due to decohesion of the matrix-particle interface or particle cracking (Maire et al., 2011). Proper modelling of the ductile damage process on the structural level requires consideration of the underlying mechanisms on a microscopic level. Damage models and associated failure criteria have been proposed (see e.g. Cockcroft and Latham (1968); Johnson and Cook (1985)) throughout the vast literature on ductile failure. Another approach is to use constitutive models that somehow reflect the microstructural evolution during plastic deformation. A widely used and reputable model was proposed by Gurson (1977) and later modified by Tvergaard (1981), the latter being referred to as the Gurson-Tvergaard (GT) model.

Micromechanical finite element models are frequently used to investigate ductile fracture mechanisms since the early numerical unit cell studies by Needleman (1972) and Tvergaard (1981, 1982). This modelling framework is attractive due to its relatively simple formulation and ability to examine the underlying failure mechanisms. Moreover, these

*Corresponding author

Email address: lars.e.dahli@ntnu.no (Lars Edvard Bryhni Dæhli)

models may be used for homogenization purposes and to calibrate constitutive relations that account for microstructural parameters, such as the GT model. A great number of studies have been devoted to calibrate porous plasticity models based on results from micromechanical simulations. Faleskog et al. (1998) employed unit cell models to fine-tune the q_i parameters of the GT model. Kim et al. (2004) and Bomarito and Warner (2015) have addressed the applicability of a homogenized material model in situations where the loading path varies with deformation. These loading paths are referred to as non-proportional.

Numerous numerical investigations have been carried out over the past few decades to study the influence of various microstructural parameters on plastic flow localization and ductile fracture properties. Void shape effects were investigated by, among other authors, Søvik and Thaulow (1997) and Steglich et al. (2008) under axisymmetric loadings. These studies demonstrate that the ductile failure strain is lower for oblate voids than for prolate voids. Steglich et al. (2008) investigated void distribution, or void spacing, effects for an Al2024 alloy by varying the unit cell aspect ratio. Their results show that, under the assumption of an axisymmetric stress state, the material ductility is reduced when the voids are closely packed in the direction normal to the major principal stress. Other studies have been devoted to the effect of particle inclusions on ductile fracture to account for void nucleation (Xu and Needleman, 1993; Steglich and Brocks, 1997).

Ductile fracture properties have shown marked dependence on the stress state. This was clearly demonstrated in the work of Bao and Wierzbicki (2004) where the failure strain for a 2024-T351 aluminium alloy was found as a non-monotonous, non-smooth function of the stress triaxiality based on results from various material experiments under global proportional loading. A local maximum of the failure strain was obtained for an average stress triaxiality of about 0.4, while a local minimum was found for a pure shear stress state. Barsoum and Faleskog (2007a) also reported a similar relation between fracture strain and stress triaxiality from combined tension-torsion experiments on Weldox steel. A great number of experimental studies have later been conducted (see e.g. Gao et al. (2009); Dunand and Mohr (2011); Faleskog and Barsoum (2013); Haltom et al. (2013); Roth and Mohr (2015)) to assess material ductility of different metal alloys under global proportional loading. These studies unanimously demonstrate that the fracture strain is dependent upon the applied stress state, both in terms of the deviatoric and hydrostatic stress. Many numerical studies have addressed the issue of plastic localization and ductile failure under proportional loading using unit cell models subjected to a wide range of stress states (Barsoum and Faleskog, 2007b, 2011; Dunand and Mohr, 2014; Tekoğlu et al., 2015). It has also become customary to generate fracture loci based on results from numerical analyses under controlled states of stress (see e.g. Gao and Kim (2006); Gao et al. (2010)). However, these studies are based upon proportional loading and do not account for the fact that the loading path may change substantially during typical deformation processes.

The influence of non-proportional loading on plastic flow and anisotropy has been addressed in previous studies, see e.g. Khan (1990) and Achani et al. (2009). Similar efforts have been made in studies predicting forming limit curves of sheet metals (Chow et al., 2001; Reyes et al., 2008). Ductile fracture properties during non-proportional stress or strain paths have also been addressed more specifically. Marini et al. (1985) performed an experimental study on load path dependence using various notched tensile specimens cut out from larger pre-strained tensile specimens. A non-linear damage rule based on the Rice-Tracey model, accounting for the change in loading path, gave results consistent to their experiments. Effects of pre-strain on ductile fracture resistance were studied numerically by Eikrem et al. (2008) in conjunction with the so-called reel-lay process of pipelines, which demonstrated that plastic pre-strain cycles influence the fracture resistance upon further loading. Recently, Papasidero et al. (2015) conducted tension-torsion experiments on an 2024-T351 aluminium alloy where the ratio between tension and torsion could be adjusted to obtain both proportional and non-proportional global loading paths. Their experimental results show that ductility is reduced for pre-tension while the opposite is true for pre-compression, the latter being confirmed also for dual phase steel sheets by Marcadet and Mohr (2015). Elaborate micromechanical investigations on non-proportional loading were not carried out until rather recently. Vadillo and Fernández-Sáez (2009) performed axisymmetric unit cell simulations where the stress triaxiality was allowed to change continuously with the effective strain imposed to the unit cell. This seems to be the first unit cell study on non-radial load cases. Also, Zhang and Skallerud (2010) investigated effects of pre-strain on void coalescence using micromechanical simulations. Their findings demonstrate that pre-strain reduces the failure strain, and that this effect is dependent upon the initial void shape, oblate voids being most susceptible to pre-strain effects. The influence of non-proportional loading paths on the fracture locus of ductile materials was later examined in a numerical study by Benzerga et al. (2012), clearly illustrating the non-uniqueness of fracture strain values for given average stress triaxialities. These numerical results were revisited experimentally by Basu and Benzerga (2015), using

both unstrained and pre-strained notched tensile specimens. The experimental and numerical fracture loci were in qualitative agreement. A recent paper by Yu et al. (2016) addresses loading path effects for generalized stress states and demonstrates that variations of both the stress triaxiality and the Lode parameter with deformation are significant for the resulting fracture loci.

Even though tensile specimens are exposed to proportional loading globally, the specimen may locally experience non-proportional loading after the onset of diffuse necking (Bao and Wierzbicki, 2004; Gao et al., 2011). This is caused by geometric constraint effects and the degree of non-proportionality varies with initial geometry of the tensile specimen. The load is in general closer to a proportional state in notched tensile specimens than in smooth tensile specimens (Basu and Benzerga, 2015). A material element occupying the centre of a smooth tensile specimen, where the ductile fracture process initiates in a typical cup-cone fracture, is especially prone to develop stress states that change with deformation. This indicates that local load path changes might be important to account for in the numerical unit cell simulations in order to examine ductile fracture properties properly.

Results from previous experimental studies have revealed a nearly linear relationship between the tensile failure strain and the initial yield stress of various aluminium alloys (Lloyd, 2003; Liu et al., 2011). Similar results have also been reported in recent studies for the aluminium alloys considered in the present work (Westermann et al., 2014; Pedersen et al., 2015) and for 6xxx aluminium alloys (Hannard et al., 2016). In the present study, the scaling of the failure strain with the initial yield stress of the material is investigated by micromechanical simulations. A large experimental database is available from previous studies on various aluminium alloys (Westermann et al., 2014; Pedersen et al., 2015), which serves as the background material for this numerical study.

First, the influence of various microstructural parameters on the ductility of four aluminium alloys is examined by the use of unit cell simulations. Specifically, effects of varying void volume fraction, void shape, and void distribution are elucidated, in addition to the effects of void nucleation due to particle decohesion. Both proportional and non-proportional loading paths are assigned to the unit cell based on selected results from numerical simulations of smooth tensile tests. The benefit of this approach is that the applied boundary conditions are in accordance with those expected to emerge locally in tensile experiments, which are widely used to assess material properties. We find that the loading path significantly alters the ductility of the investigated materials. Also, the various microstructural parameters that we examine are seen to scale the fracture strain curves obtained from unit cell simulations. Second, the GT model is used to simulate tests on smooth and notched tensile specimens and to validate its applicability for the investigated materials. The correspondence with experimental data is better for the smooth specimens than for the notched specimens, for which the global response is overestimated. Despite the inconsistencies in the stress-strain response for the notched specimens, the onset of failure is seen to be within acceptable agreement when the material response is governed by the GT model. Lastly, the initial porosity will be calibrated from unit cell simulations to provide similar failure strain values as in the tensile experiments. These calibrated porosities are then used in an additional series of tensile specimen simulations with the GT model. We found that the fitted porosity values only led to minor improvements on the stress-strain curves, but improved the ductility predictions of the GT model for all the materials and specimens investigated in this study.

2. Materials and experiments

Material data from tensile experiments carried out on four aluminium alloys in a previous study by Pedersen et al. (2015) are used in all numerical simulations throughout this paper. In the subsequent sections, the materials are referred to as Al0.2Fe, Al0.8Fe, Al1.2Mn, and AlMgSi. Details regarding the chemical composition of the materials can be found in recent papers dealing with the experimental procedure (Westermann et al., 2014; Pedersen et al., 2015) and will not be repeated here. The aluminium alloys were provided as DC-cast (direct chilled) extrusion ingots produced at Hydro Aluminium R&D Sunndal. Before testing, the alloys were homogenized and subjected to a two-stage processing route consisting of i) extrusion, and ii) cold rolling and recrystallization.

The experimental program that forms the basis of the present work consists of triplicate quasi-static tensile tests performed on smooth and notched axisymmetric specimens oriented along the rolling direction of the alloys (Pedersen et al., 2015). The spread between parallel tests was negligible for all materials. A two-term Voce work-hardening rule on the form

$$\sigma_{\mathrm{M}} = \sigma_0 + \sum_{i=1}^{2} Q_i \left(1 - \exp(-C_i p)\right) \tag{1}$$

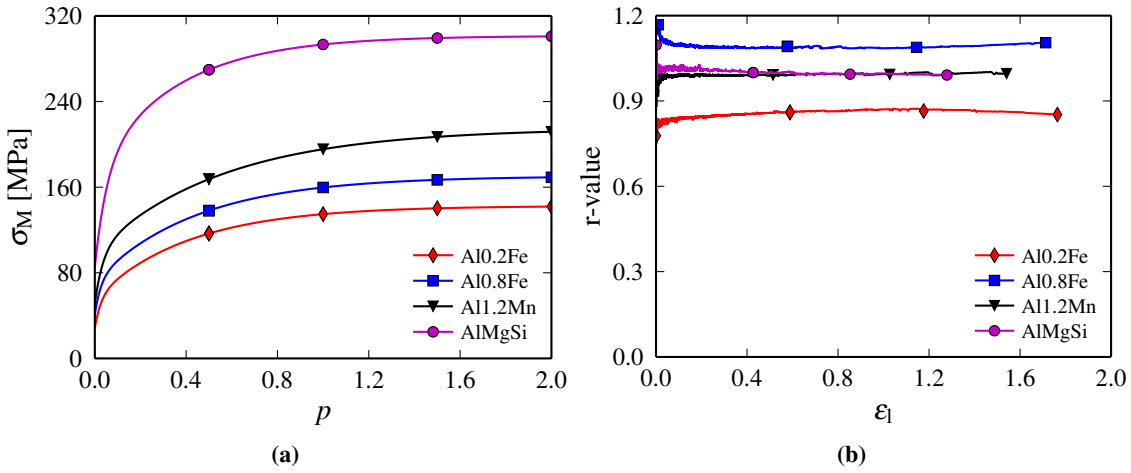

Figure 1: Figure showing the (a) work-hardening curve and (b) the r-values for representative tensile tests on smooth specimens of each material.

was subsequently fitted to material data from experiments on the smooth tensile bars. Symbols σ_M and p denote the material flow stress and the accumulated plastic strain, respectively, the latter being defined by

$$p = \int_0^t \sqrt{\frac{2}{3}\mathbf{D}^p : \mathbf{D}^p}\,dt \tag{2}$$

where $\mathbf{D}^p$ is the plastic rate-of-deformation tensor. The resulting material parameters are repeated in Table 1 for convenience and will be used throughout this paper. Work-hardening curves for the four aluminium alloys are shown in Figure 1a. Pedersen et al. (2015) reported excellent correspondence between the fitted work-hardening rule and the experimental data. It is noted that the calibrated work-hardening curves are valid also for large strains, since experimental data from the tensile tests up to material failure, defined as the maximum of the true tensile stress-strain curve, were used in the calibration process.

Table 1: Yield strength and work-hardening parameters of the four aluminium alloys.

Material	σ_0 [MPa]	Q_1 [MPa]	C_1	Q_2 [MPa]	C_2
Al0.2Fe	28.26	28.05	37.31	86.26	2.41
Al0.8Fe	40.96	31.50	37.79	97.89	2.22
Al1.2Mn	51.15	48.51	27.98	115.49	1.77
AlMgSi	85.31	92.33	19.03	124.04	2.72

Figure 1b shows the r-values, defined as the ratio between transverse strain components, against the longitudinal strain (ε_l) from representative tensile experiments for each of the four aluminium alloys. These results indicate that the Al1.2Mn, and AlMgSi alloys are quasi-isotropic after the second processing step (Pedersen et al., 2015). For the Al0.2Fe and Al0.8Fe alloys the r-value is not unity, and the alloys cannot be considered isotropic in that sense. However, the orientation distribution functions for the Al0.2Fe alloy and Al0.8Fe alloys show a maximum intensity of 5.1 and 7.9, respectively, indicating that these alloys have a weak crystallographic texture.

3. Numerical models

A combination of numerical models will be used in this study; i) tensile specimen models on the macroscopic scale, and ii) unit cell models on the microscopic scale. All numerical models are developed within a finite element (FE) framework using the implicit solver of the commercial software ABAQUS 6.13 (Abaqus, 2013).

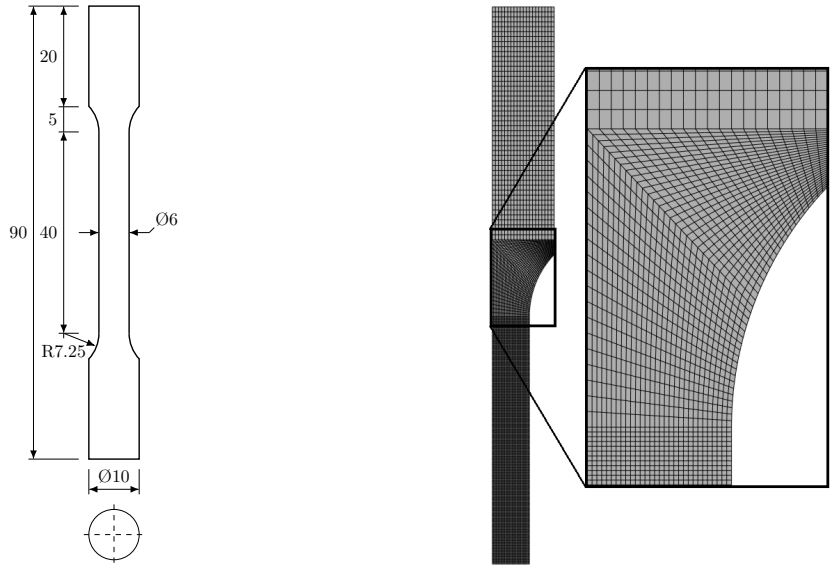

Figure 2: Sketch of the geometry and the corresponding FE model for the smooth tensile specimen. The figures show (a) geometry of smooth specimen, and (b) mesh used for spatial discretization. The transition mesh applied in the specimen shoulder is shown in the magnified view. All units are in mm.

3.1. Tensile specimens

Three different tensile specimen geometries are used in the present study; one smooth specimen geometry and two different notched specimen geometries with initial notch radii of $R = 2.0$ mm (R2.0) and $R = 0.8$ mm (R0.8), respectively. Due to the axisymmetry of the tensile specimens and the presumed quasi-isotropic properties of all aluminium alloys considered in this work, the tensile specimens were modelled using axisymmetric finite element models. Symmetry conditions were employed, such that only the upper half of the tensile specimens was modelled. The geometry of all three tensile specimens used in the study and their corresponding finite element model are shown in Figures 2-4.

The material response of the tensile specimens was modelled in a hypoelastic-plastic framework using two different yield descriptions; the conventional J_2 (von Mises) flow theory, and the GT model accounting for material softening due to void growth. The J_2 flow theory is given by the yield function

$$\phi = \sigma_{\text{eq}} - \sigma_{\text{M}} \leq 0 \tag{3}$$

while the GT model is described by the yield function

$$\Phi = \left(\frac{\Sigma_{\text{eq}}}{\sigma_{\text{M}}}\right)^2 + 2q_1 f \cosh\left(\frac{3}{2} q_2 \frac{\Sigma_{\text{h}}}{\sigma_{\text{M}}}\right) - \left(1 + q_3 f^2\right) \leq 0 \tag{4}$$

where $\Sigma_{\text{eq}} = \sqrt{3J_2}$ is the macroscopic equivalent stress, σ_{M} is the matrix material flow stress, $\Sigma_{\text{h}} = \Sigma_{kk}/3$ is the hydrostatic stress, f is the porosity, and q_i are the material parameters introduced by Tvergaard (1981). In both descriptions of plastic flow, we use the associated flow rule and isotropic hardening corresponding to the two-term Voce rule given by Equation (1) with the material parameters listed in Table 1. Note that for an associated flow rule, the plastic rate-of-deformation tensor is determined from

$$\mathbf{D}^{\text{p}} = \dot{\Lambda} \frac{\partial \Phi}{\partial \boldsymbol{\Sigma}} \tag{5}$$

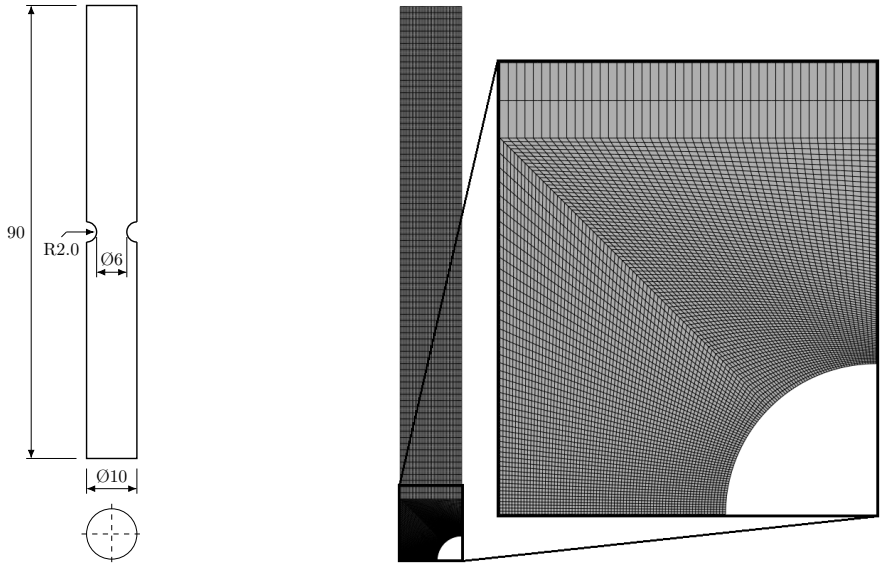

(a) **(b)**

Figure 3: Sketch of the geometry and the corresponding FE model for notched tensile specimen with notch radius R = 2.0 mm. The figures show (a) geometry of specimen, and (b) mesh used for spatial discretization. The transition mesh applied in the notch region is shown in the magnified view. All units are in mm.

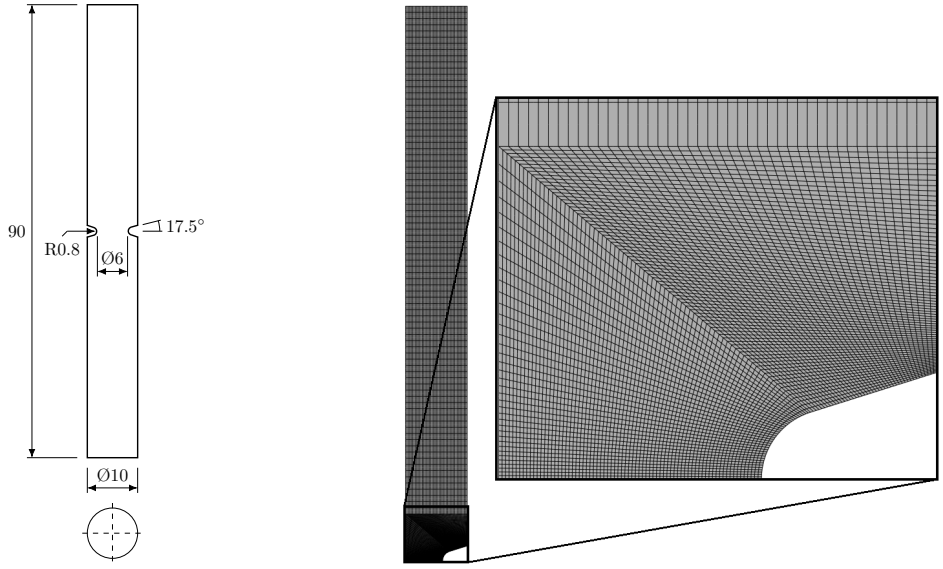

(a) **(b)**

Figure 4: Sketch of the geometry and the corresponding FE model for notched tensile specimen with notch radius R = 0.8 mm. The figures show (a) geometry of specimen, and (b) mesh used for spatial discretization. The transition mesh applied in the notch region is shown in the magnified view. All units are in mm.

where $\dot{\Lambda}$ is the plastic parameter. In the case of J_2 flow theory, the accumulated plastic strain is calculated from Equation (2). When the GT model is used, only the matrix material contributes to plastic dissipation. Thus, the accumulated plastic strain in this case is calculated from

$$p = \int_0^t \frac{\boldsymbol{\Sigma} : \mathbf{D}^{\mathrm{p}}}{(1-f)\,\sigma_{\mathrm{M}}} \mathrm{d}t \tag{6}$$

The evolution of porosity with continued plastic deformation is in the GT model governed by void growth according to

$$\dot{f} = (1-f)\,\mathrm{tr}\mathbf{D}^{\mathrm{p}} \tag{7}$$

We note that void coalescence is not accounted for in the GT model and the porous plasticity modelling undertaken in the present paper is only concerned with the void growth phase. However, void coalescence criteria that are in the spirit of the unit cell calculations are proposed in literature (see e.g. Benzerga and Leblond (2010) and references therein) and recently developed on rigorous grounds (Benzerga and Leblond, 2014).

To compare the results with experiments (Pedersen et al., 2015), the tensile stress-strain response is determined using the total force and diameter reduction data extracted from numerical simulations of the tensile specimens. The true stress and logarithmic strain are evaluated from

$$\sigma_{\mathrm{t}} = \frac{4F}{\pi D^2}, \quad \varepsilon_{\mathrm{l}} = 2\ln\left(\frac{D_0}{D}\right) \tag{8}$$

where F is the tensile force, and D_0 and D correspond to the reference diameter and the current diameter of the minimum cross-section of the specimen, respectively. Note that these relations presume that the cross-section remains circular and that plastic deformation is isochoric. Also, we should note that the true stress defined by Equation (8) is a net axial stress, which after necking deviates from the equivalent stress due to lateral stress components.

The loading path applied to the unit cell (described in the Section 3.2.1) is governed by the stress triaxiality evolution obtained in the critical element of the smooth tensile specimen. The stress triaxiality is given on the usual form

$$T = \frac{\sigma_{\mathrm{h}}}{\sigma_{\mathrm{eq}}} \tag{9}$$

In the unit cell study, the stress triaxiality will be applied either as an averaged value or as a continuous function of the equivalent strain. To this end, the strain-averaged stress triaxiality value is determined from

$$\bar{T} = \frac{1}{\varepsilon_{\mathrm{eq}}^{\mathrm{c}}} \int_0^{\varepsilon_{\mathrm{eq}}^{\mathrm{c}}} T \mathrm{d}\varepsilon_{\mathrm{eq}} \tag{10}$$

where $\varepsilon_{\mathrm{eq}} = \sqrt{\frac{2}{3}\boldsymbol{\varepsilon}' : \boldsymbol{\varepsilon}'}$ is an equivalent strain measure, $\boldsymbol{\varepsilon}'$ is the deviatoric strain tensor, and $\varepsilon_{\mathrm{eq}}^{\mathrm{c}}$ denotes the equivalent strain at material failure. In the smooth tensile tests, material failure is assumed to coincide with the point of maximum true stress (Pedersen et al., 2015). The corresponding logarithmic strain is referred to as failure strain and determined from $\varepsilon_{\mathrm{l}}^{\mathrm{c}} = \varepsilon_{\mathrm{l}}\left(\frac{d\sigma_t}{d\varepsilon_{\mathrm{l}}} = 0\right)$. We note that final fracture of the tensile specimens occurs shortly after the point of maximum true stress, which implies that this point may be assumed as the onset of void coalescence in the middle part of the specimen. Hence, we define the coalescence strain in the smooth tensile simulations ($\varepsilon_{\mathrm{eq}}^{\mathrm{c}}$) as the value of the equivalent strain in the critical element when the logarithmic strain (as calculated from the latter relation in Equation (8)) in the neck of the simulated specimens reaches the experimental value (Pedersen et al., 2015). In the case of axisymmetric models, the equivalent strain reduces to

$$\varepsilon_{\mathrm{eq}} = \frac{2}{3}|\varepsilon_{rr} - \varepsilon_{zz}| \tag{11}$$

since $\varepsilon_{rr} = \varepsilon_{\theta\theta}$. The equivalent strain in the critical element is thus evaluated by extracting the logarithmic strain components in longitudinal and radial direction from the simulation and use of Equation (11). The application of a constant stress triaxiality value corresponds to a proportional loading path. In analyses where non-proportional loading paths are assigned to the unit cell, a 10^{th}-order polynomial is fitted to the stress triaxiality evolution in the critical

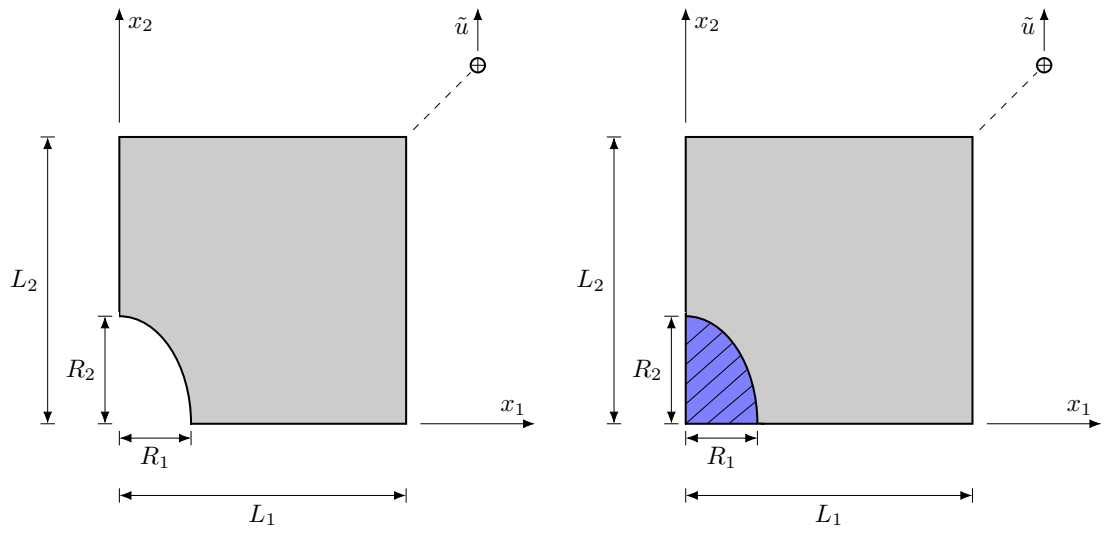

(a) **(b)**

Figure 5: Illustration of the axisymmetric unit cell with (a) void, and (b) particle. The loading is applied by prescribing the displacement $\tilde{u}$ in the dummy node located outside the cell.

element. Thus, the stress triaxiality is a continuous function of the equivalent strain on the form

$$T(\varepsilon_{\text{eq}}) = a_0 + \sum_{i=1}^{10} a_i \varepsilon_{\text{eq}}^i \tag{12}$$

where a_0, a_1, ... , a_{10} are constants to be determined in the curve fit procedure.

3.2. Unit cell

Representative volume elements (RVE) are widely used to examine the material response on an intermediate scale, often referred to as a mesoscopic scale. In the present study, axisymmetric unit cells are used to approximate a periodic distribution of material elements containing spheroidal voids or particles, as illustrated in Figures 5a and 5b, respectively. Note that the axisymmetric RVE is not a true periodic structure. However, these types of unit cell models have been extensively used in literature, see e.g. Tvergaard (1982), Becker et al. (1989), Koplik and Needleman (1988), Brocks et al. (1995, 1996), and Søvik and Thaulow (1997).

Due to symmetry conditions only the upper half of the unit cell is modelled, as illustrated in Figure 5. The geometry of the unit cell is defined by the void aspect ratio w, cell aspect ratio λ, and the void volume fraction f, with initial values given by

$$w_0 = \frac{R_2}{R_1}, \quad \lambda_0 = \frac{L_2}{L_1}, \quad f_0 = \frac{2R_1^2 R_2}{3L_1^2 L_2} \tag{13}$$

Prescription of w_0, λ_0 and f_0 uniquely defines the initial cell geometry. These parameters will be varied separately in a parameter study presented in Section 4.2 to elucidate their effects on the ductility.

The cell boundaries are constrained to remain straight throughout the analyses. Thus, the macroscopic true strain components applied to the unit cell are determined from

$$E_{11} = \ln\left(\frac{l_1}{L_1}\right), \quad E_{22} = \ln\left(\frac{l_2}{L_2}\right), \quad E_{33} = E_{11} \tag{14}$$

where l_i and L_i denote the current and reference lengths of the unit cell along the coordinate axes x_i, respectively, while

the latter relation derives from the axisymmetric conditions. An equivalent strain measure is defined such that

$$E_{\mathrm{eq}} = \frac{2}{3}|E_{22} - E_{11}| \tag{15}$$

The hydrostatic stress and the von Mises equivalent stress are readily expressed in terms of the macroscopic Cauchy stress components

$$\Sigma_{\mathrm{h}} = \frac{2\Sigma_{11} + \Sigma_{22}}{3}, \quad \Sigma_{\mathrm{eq}} = |\Sigma_{22} - \Sigma_{11}| \tag{16}$$

where the condition that $\Sigma_{11} = \Sigma_{33}$ has been invoked. Note that the macroscopic stress and strain rate components are equal to their corresponding volume averaged quantities (Hill, 1967).

3.2.1. Controlling the macroscopic loading path

Different methods of maintaining a proportional stress state have been proposed in the literature, see e.g. Lin et al. (2006). In this work, we will adopt a method to control the macroscopic stress state on the unit cell which is based on application of appropriate kinematic boundary conditions. This method was first proposed by Faleskog et al. (1998) in the case of plane strain conditions with constant in-plane biaxial stress ratios. Kim et al. (2004) recast the method in an axisymmetric form. Vadillo and Fernández-Sáez (2009) have extended the method to account for non-proportional loading paths. The objective of the method is to control the stress state in a dummy node where a uniaxial stress state prevails. A brief overview of the method will be given below.

The ratio between the stress components is introduced on the form

$$\rho = \frac{\Sigma_{11}}{\Sigma_{22}} \tag{17}$$

such that the stress triaxiality given by Equation (9) can be expressed as

$$T = \frac{\Sigma_{\mathrm{h}}}{\Sigma_{\mathrm{eq}}} = \frac{1 + 2\rho}{3\,|1 - \rho\,|}, \quad \Sigma_{22} \geq 0 \tag{18}$$

using the expressions found in Equation (16). Consequently, from a prescription of the stress triaxiality level, the stress ratio is explicitly calculated using

$$\rho = \frac{3T - 1}{3T + 2} \tag{19}$$

in the case of generalized tension where $\rho \leq 1$ when $T > -\frac{2}{3}$, which encompasses all relevant stress triaxiality levels in the present study.

The total deformation power of the unit cell may be expressed as (Hill, 1967)

$$\begin{aligned} \dot{W}_{\mathrm{d}} &= V\Sigma_{ij}\dot{E}_{ij} = 2V\Sigma_{11}\dot{E}_{11} + V\Sigma_{22}\dot{E}_{22} \\ &= P_1\dot{E}_{11} + P_2\dot{E}_{22} \end{aligned} \tag{20}$$

where V denotes the total volume of the cell in the current configuration. Generalized force terms $P_1 = 2V\Sigma_{11}$ and $P_2 = V\Sigma_{22}$ have been introduced for notational convenience. Hence, the ratio between the generalized force components are

$$\psi = \frac{F_1}{F_2} = \frac{2\Sigma_{11}}{\Sigma_{22}} = 2\rho \tag{21}$$

The generalized force components may now be recast in vector form

$$\mathbf{P} = \begin{bmatrix} P_1 \\ P_2 \end{bmatrix} = P_2 \begin{bmatrix} \psi \\ 1 \end{bmatrix} \tag{22}$$

Appropriate displacement boundary conditions are applied in a transformed coordinate system in which the

macroscopic stress state is uniaxial. To this end, a coordinate transformation is introduced such that

$$\mathbf{P} = \mathbf{Q}\tilde{\mathbf{P}}, \quad \dot{\mathbf{E}} = \mathbf{Q}\dot{\tilde{E}} \tag{23}$$

where $\mathbf{Q}$ is an orthonormal tensor on the form (Faleskog et al., 1998; Kim et al., 2004; Vadillo and Fernández-Sáez, 2009)

$$\mathbf{Q} = \begin{bmatrix} \beta_2 & \beta_1 \\ -\beta_1 & \beta_2 \end{bmatrix} \tag{24}$$

The coefficients are expressed in terms of the stress ratios on the form

$$\beta_1 = \frac{\psi}{\sqrt{1+\psi^2}}, \quad \beta_2 = \frac{1}{\sqrt{1+\psi^2}} \tag{25}$$

The global strain rate components are given by

$$\dot{E}_{11} = \frac{\dot{l}_1}{l_1} = \frac{\dot{u}_1}{L_1 + u_1}, \quad \dot{E}_{22} = \frac{\dot{l}_2}{l_2} = \frac{\dot{u}_2}{L_2 + u_2} \tag{26}$$

Consequently, the displacement rates on the unit cell boundaries are determined from

$$\dot{u}_1 = (L_1 + u_1)\,\dot{E}_{11} = (L_1 + u_1)\left[\beta_2\dot{\tilde{E}}_{11} + \beta_1\dot{\tilde{E}}_{22}\right] \tag{27}$$

$$\dot{u}_2 = (L_2 + u_2)\,\dot{E}_{22} = (L_2 + u_2)\left[-\beta_1\dot{\tilde{E}}_{11} + \beta_2\dot{\tilde{E}}_{22}\right] \tag{28}$$

These equations constitute a set of non-linear constraints that govern the macroscopic loading of the unit cell. In order to obtain a uniaxial stress state in the dummy node, the boundary conditions are given on the form

$$\tilde{P}_1 = 0, \quad \dot{\tilde{E}}_{22} = \dot{\tilde{E}}_0 \tag{29}$$

In the finite element procedure with Abaqus/Standard, this can be accomplished by assigning a non-zero displacement ($\tilde{u}_2 = \tilde{u}$) to the second degree-of-freedom in a dummy node, as shown in Figure 5. The other degrees-of-freedom of the dummy node are allowed to move arbitrarily such that the stress state remains uniaxial. A Multi Point Constraint (MPC) user subroutine (Abaqus, 2013) is used to drive the deformation of the unit cell boundaries according to the non-linear constraints in Equations (27) and (28). Note that in simulations where the stress triaxiality changes with the equivalent strain, described by Equation (12), the stress ratio given in Equation (19) changes accordingly throughout the simulation and is updated in the MPC routine.

3.2.2. Cohesive properties of particle-matrix interface

Void nucleation by particle debonding is important for material ductility and toughness, as demonstrated by Xu and Needleman (1993). In order to investigate the effects of particle decohesion on ductile fracture on a microscopic level, unit cells with a particle embedded in the matrix material are modelled to represent a homogeneous distribution of spheroidal particles. A cohesive surface interaction property is used for the particle-matrix interface. The behaviour of the cohesive surface is approximated by an uncoupled bilinear traction-separation law. This type of cohesive behaviour has also been employed by Segurado and Llorca (2005), Suh et al. (2009), and Williams et al. (2012). Decohesion of the matrix-particle interface is governed by an energy criterion on the form

$$\Gamma^{\mathrm{c}} = \frac{1}{2} t^0_{\mathrm{eff}} \delta^{\mathrm{c}}_{\mathrm{eff}} \tag{30}$$

where t^0_{eff} and $\delta^{\mathrm{c}}_{\mathrm{eff}}$ are effective values of traction and separation at onset of damage and total failure, respectively. The decohesion energy Γ^{c} is an input parameter in the finite element model. For details regarding the cohesive surface model, we refer the reader to Section 37.1.10 of the Abaqus Analysis Users Manual (Abaqus, 2013).

We note that other investigations, e.g. Xu and Needleman (1993) and McVeigh et al. (2007), use an exponential traction-separation law to describe the cohesive behaviour in the normal direction at the particle-matrix interface.

This is in accordance with atomistic calculations of binding-energy-separation for different metals and bimetallic surfaces (Rose et al., 1981, 1983; Ferrante and Smith, 1985). The choice of using a linear traction-separation law in the present study is motivated by the lack of experimental data for the cohesive properties of the interface between iron-rich primary particles and the aluminium matrix material. We believe that the particle shape and the roughness of the interface layer have large influence on the interface properties. This is related to the scale at which we model the problem. The mesoscopic scale represents an intermediate level that involves a huge amount of individual atoms, and their bulk characteristics might not resemble those of the individual atoms. We are not certain that the bilinear traction-separation law is a realistic model for the particle-matrix interface, but it offers a fairly simple way of studying possible effects of void nucleation. An overview of various cohesive zone models and studies where these have been employed is given by Chandra et al. (2002).

4. Results and discussion

The numerical work conducted in this paper is divided into three parts:

1. Simulations of smooth tensile tests with the J_2 flow theory have been used to extract the loading path from the critical element.
2. Proportional and non-proportional loading paths are assigned to the unit cell in order to examine the ductility of the four studied aluminium alloys. Onset of void coalescence is chosen as an appropriate measure of ductility and is defined as the point where the global unit cell deformation shifts into a uniaxial straining mode.
3. The J_2 flow theory and the GT model are used in simulations of smooth and notched tensile specimens. Results from these simulations are then compared with experimental data from Pedersen et al. (2015) to assess their predictive capabilities.

Results obtained in the different parts of the study are presented sequentially in the next sections. The implicit finite element solver Abaqus/Standard 6.13 was used in all simulations.

4.1. Smooth tensile specimens with J_2 flow theory

The local loading path of the specimen cannot be found from experimental data and it is necessary to rely on numerical simulations of the experiments for local measurements of field quantities within the material body. Specifically, we extract the local loading and deformation history from the critical element located in the middle of the specimen where the fracture initiates in a typical cup-cone fracture. This corresponds to the lower leftmost element of the meshed model shown in Figure 6a. Since smooth tensile tests are commonly used to assess material properties, such as ductility, only numerical simulations of smooth tensile specimens are used to extract loading paths for subsequent application in unit cell simulations. To this end, we use the numerical model of the smooth tensile specimen presented in Section 3.1. We used an approximate element size of 0.1 mm in the gauge section of the specimen, and the local quantities from these simulations are then understood as averaged over a number of grains. The resulting mesh is shown in Figure 2b. Quadratic elements with reduced integration (CAX8R) were employed in all simulations.

Table 2: The 0.2% proof stress, logarithmic strain at failure in smooth tensile tests and corresponding equivalent strain values extracted from the critical element, and the averaged stress triaxiality values for the four aluminium alloys.

Material	$\sigma_{0.2}$ [MPa]	ε_1^c	ε_{eq}^c	$\bar{T}$
Al0.2Fe	30.69	1.766	1.832	0.661
Al0.8Fe	43.69	1.713	1.780	0.651
Al1.2Mn	54.20	1.541	1.659	0.608
AlMgSi	89.15	1.279	1.412	0.624

The diameter reduction in the neck and the total reaction force of the specimen were extracted from the simulations. True stress and logarithmic strain were further calculated from these values using the expressions in Equation (8). As mentioned in Section 3.1, Pedersen et al. (2015) defined failure strain as the value of logarithmic strain at the point of maximum true stress, denoted ε_1^c in Table 2. In the simulations of the smooth tensile specimens, we use these failure

strain values to define material failure. At the same instant we also extract the equivalent strain in the critical element, denoted ε_{eq}^{c}. This value is referred to as the coalescence strain and defines the local effective deformation of an RVE located in the middle part of the tensile specimen. Failure strain and coalescence strain values for the different materials are given in Table 2. A representative deformed mesh for the Al0.2Fe alloy at the onset of material failure is shown in Figure 6a.

The evolution of stress triaxiality with equivalent strain in the critical element was extracted from the simulations. Note that since the elements contain four integration points, the stress and strain components are volume averaged over these integration points. The stress triaxiality and equivalent strain are calculated from the volume averaged stress and strain quantities. This volume averaging procedure is invoked so that the unit cell model represents the entire critical element. Strain-averaged stress triaxiality values for the different aluminium alloys were calculated from Equation (10) by numerical integration. The corresponding values are given in Table 2. A 10^{th}-order polynomial of the form given in Equation (12) was fitted to the numerical data to represent the non-proportional loading applied to the unit cell. Figure 6b shows that the polynomial describes the stress triaxiality evolution from the simulations perfectly. We also observe a similar evolution of stress triaxiality for the Al0.2Fe, Al0.8Fe, and Al1.2Mn alloys. This is possibly because their strain hardening properties are relatively similar, which may be inferred from Figure 1a. The AlMgSi alloy is seen to develop higher stress triaxiality levels at lower equivalent strain, which is most likely caused by geometric finite strain effects, as discussed by Pardoen (2006). The AlMgSi alloy hardens faster than the other three alloys for small values of plastic strain, but reaches flow stress values close to the saturation value for moderate plastic strain. As the hardening rate diminishes, a sharper neck develops in the tensile specimen. In turn, this increases the stress triaxiality in the necked region due to the imposed geometric constraint. The Al0.2Fe, Al0.8Fe, and Al1.2Mn alloys harden more slowly in the beginning, however maintaining a higher work-hardening rate for larger values of plastic strain. Thus, the hardening capacity is somewhat increased for these three alloys, promoting a more diffuse neck and lowering the stress triaxiality levels in the necked region. This geometric effect also influences the predicted ductility of the tensile specimens, which is apparent from the failure strain values presented in Table 2.

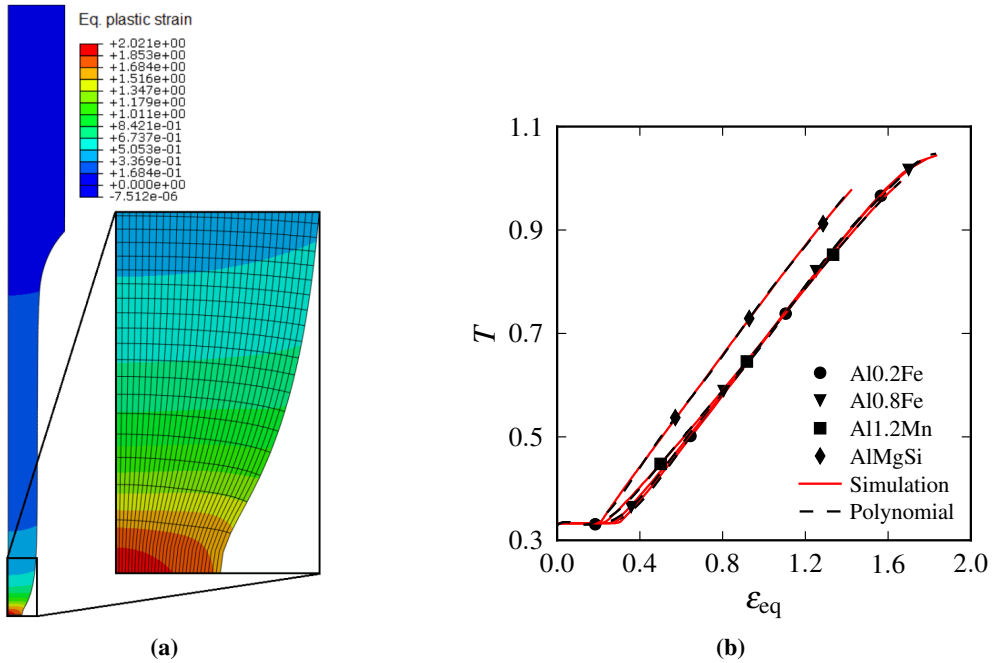

Figure 6: Figure showing (a) representative deformed mesh with fringes of equivalent plastic strain for the Al0.2Fe smooth tensile specimen at the onset of material failure, and (b) the stress triaxiality evolution from the critical element in the smooth tensile simulations plotted against the equivalent strain. Curves from the simulation and from the fitted polynomial are shown for all four aluminium alloys.

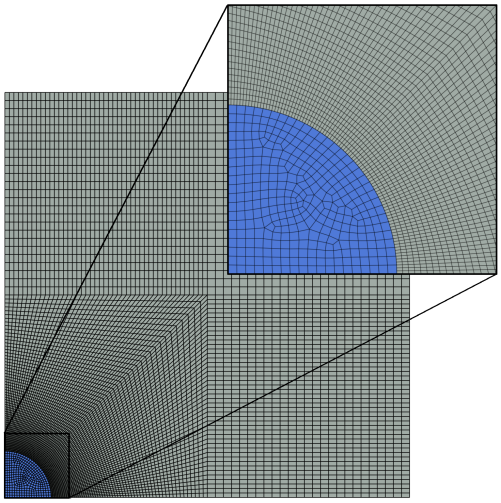

Figure 7: Mesh used in analyses with $f_0 = 0.001$, $w_0 = 1$ and $\lambda_0 = 1$. Note that this mesh contains a particle (indicated by blue color) whereas in most simulations the particle is replaced by a void. A magnified view of the mesh refinement along the particle/matrix interface is also shown.

4.2. Micromechanical simulations

Proportional and non-proportional loading paths corresponding to the critical element in smooth tensile specimens were applied in a series of unit cell simulations. The mesh depended slightly on the initial geometry of the specimen, but the number of elements was approximately 10.000 in all simulations. Linear axisymmetric elements with selectively reduced integration (CAX4) were used in all analyses. Figure 7 shows the mesh for an initial cell geometry defined by $f_0 = 0.001$, $w_0 = 1$ and $\lambda_0 = 1$. A particle is included in this model to show the particle mesh, as indicated by the blue-tinted region. A magnified view of the particle-matrix interface is presented to illustrate the mesh refinement applied in this part of the model.

Table 3: Elastic properties of the matrix and particle materials.

Material	E [GPa]	ν
Matrix	70	0.3
Particle	210	0.3

The matrix was modelled as an isotropic elasto-plastic material governed by the J_2 flow theory with associative flow and isotropic hardening, described by the two-term Voce rule in Equation (1) using material parameters from Table 1. Elastic properties for the matrix material are found in Table 3. In simulations where void nucleation has been examined, we exchanged the void in the unit cell model with a particle. The particle was modelled as an elastic inclusion with the initial aspect ratio set to unity ($w_0 = 1$). Elastic properties for the particle are listed in Table 3. A small-sliding contact formulation was used on the particle-matrix interface. These simulations adopt a cohesive surface definition for the particle-matrix interface behaviour, as described in Section 3.2.2. The cohesive surface properties were chosen such that a specific surface energy of $\Gamma^c = 50$ J/m^2 was obtained when the matrix detaches from the particle. Specifically, we set the normal and shear traction components for damage initiation to values of $t_n^0 = 100$ MPa and $t_s^0 = 20$ MPa, respectively, which facilitates earlier onset of damage in shear. This is merely a choice we made in order to avoid numerical problems and is not based on physical evidence. Viscous regularization was employed in all analyses including a particle to preclude convergence difficulties. The regularization coefficient was set to $\mu = 1 \cdot 10^{-5}$ s (Abaqus, 2013). We note that the debonding energy of the cohesive surface is on the same order of magnitude as that used by Bonfoh and Lipinski (2007) in their study of ductile damage by particles debonding in an aluminium alloy reinforced by SiC particles.

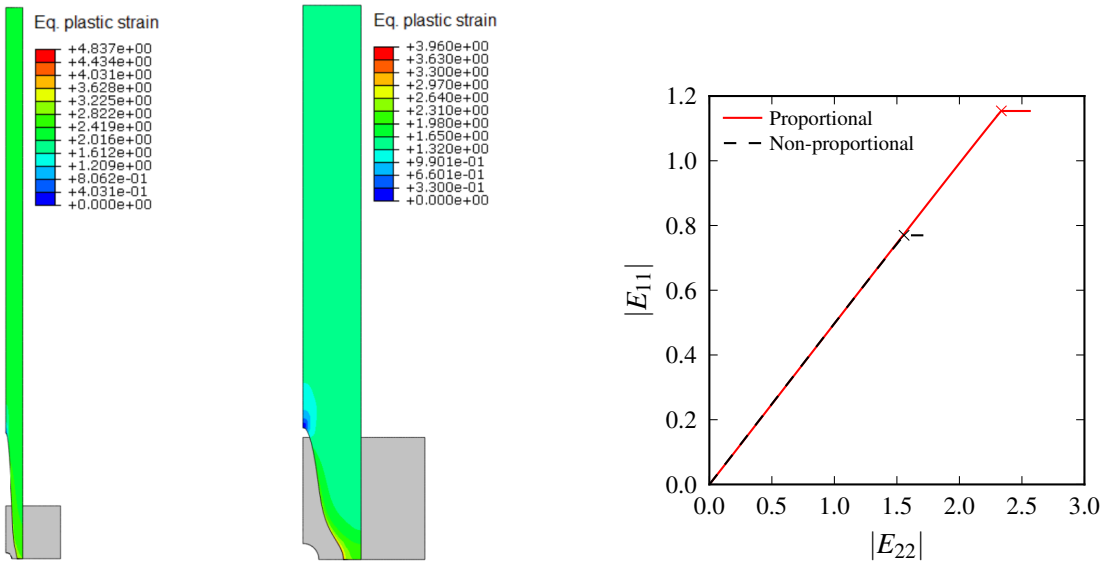

Figure 8: Figure showing the unit cell in the undeformed configuration and at the onset of void coalescence for the AlMgSi alloy. Fringes of equivalent plastic strain are plotted for (a) proportional loading, and (b) non-proportional loading. Note that the scale is different between the two since the proportional loading leads to greater extension of the unit cell. Figure (c) shows the transverse strain E_{11} against the longitudinal strain E_{22} in unit cell simulations (a) and (b). The onset of coalescence is marked by a cross.

Onset of void coalescence is assumed to occur as the unit cell deformation shifts to a uniaxial straining mode, which has been suggested by a number of authors (see e.g. Koplik and Needleman (1988) or Kim et al. (2004)). The evolution of transverse strain with longitudinal strain from unit cell simulations for the AlMgSi alloy under proportional and non-proportional loading is shown in Figure 8c, where the onset of void coalescence is marked by a cross. The equivalent strain at the onset of the uniaxial straining mode is denoted coalescence strain throughout this paper when results from unit cell simulations are presented and discussed. Deformed configurations of the AlMgSi alloy, with fringes of equivalent plastic strain, just after the onset of void coalescence are shown in Figures 8a and 8b for proportional and non-proportional loading, respectively.

4.2.1. Comments on matrix strain hardening effects

Initially, constant stress triaxiality levels of $T = 0.58$, 0.65, 1.0 and 1.5 were maintained for all four alloys to elucidate effects of strain hardening under identical loading situations. The unit cells were modelled with a pre-existing void in these analyses and an initial cell geometry corresponding to $f_0 = 0.001$, $w_0 = 1$, and $\lambda_0 = 1$. Coalescence strain values obtained from the unit cell simulations are compared with corresponding coalescence strain values extracted from the critical element in simulations of the smooth tensile specimen. This is shown in Figure 9. We remark that the presented coalescence strain values from the smooth tensile specimen simulations are the equivalent strain values extracted from the critical element at material failure, as discussed in Section 4.1. The dashed lines, referred to as failure strain curves throughout this paper, represent linear best-fit curves to the coalescence strain values as functions of the 0.2% proof stress. Failure strain curves from experimental data for the aluminium alloys used in the present study were presented in a previous study by Pedersen et al. (2015).

The results presented in Figure 9 show that the failure strain curves obtained from unit cell simulations with constant stress triaxiality levels are nearly flat. This indicates that the ductility of the four aluminium alloys is hardly affected by material strain hardening when the stress triaxiality is kept fixed for all materials. Hence, the intrinsic effect of strain hardening on the predicted ductility is low. However, it is important to bear in mind that strain hardening directly influences the flow stress and plastic localization. Increased work-hardening capacity delays the void coalescence process and smooths out plastic strain gradients. As discussed in Section 4.1, the stress triaxiality level is linked to this geometric finite strain effect imposed by the necking down of the intervoid ligament. Stress triaxiality has been

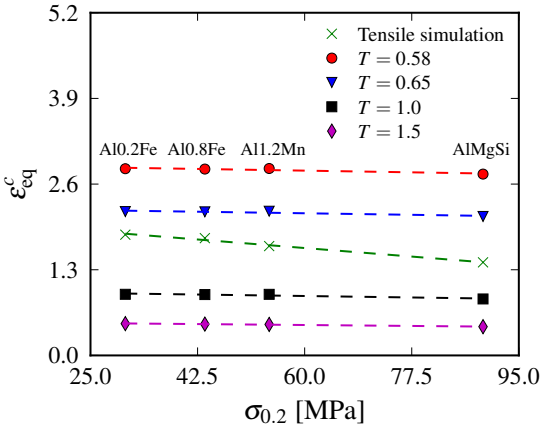

Figure 9: Failure strain curves from unit cell simulations under constant stress triaxiality compared with experimental data.

shown to greatly influence the ductility in a vast number of studies (see e.g. Bao and Wierzbicki (2004)). Since the global stress triaxiality level of the unit cell is kept fixed, it is expected that the difference in work-hardening capacity of the alloys causes the spatial stress and strain fields to differ between the various aluminium alloys. Specifically, a larger work-hardening capacity decreases the void growth rate. However, the effects of these local fluctuations of the field variables within the unit cell seem less important for the predicted ductility than the geometric finite strain effect, which is precluded by maintaining a fixed stress triaxiality level. With this in mind, we remark that this result should not be interpreted as evidence of the ductile fracture properties being independent of the work-hardening from a macroscopic perspective. However, it suggests that fracture loci computed from unit cell simulations using a wide range of proportional stress states might appear similar even though the materials differ substantially in terms of tensile properties.

4.2.2. Proportional loading path

We applied the strain-weighted stress triaxiality values from the smooth tensile simulations, given in Table 2, to the unit cell. The reference values for the cell geometry are $f_0 = 0.001$, $\lambda_0 = 1$, and $w_0 = 1$, with a pre-existing void contained in the model. Four separate parameter studies were carried out to investigate the effect of the microstructural parameters on ductile failure.

Linear failure strain curves and coalescence strain values for the different alloys are shown in Figure 10. As readily observed, all parameters essentially affect the ductility in the same manner by effectively shifting the failure curves. More interesting, however, is their slope. From the experimental data, we see that the largest coalescence strain is obtained for Al0.2Fe, with monotonically decreasing values for the Al0.8Fe, Al1.2Mn, and AlMgSi alloys. The trend is opposite in the unit cell simulations, where Al1.2Mn has the largest coalescence strain value, and the AlFe alloys are least ductile. In light of the average stress triaxiality values from Table 2, this is not very surprising since larger stress triaxiality values lowers the ductile fracture strain.

These erroneous results can obviously be remedied in a number of ways by changing the microstructural parameters appropriately. However, scanning electron micrographs show quite similar particle distributions in all the aluminium alloys considered here (Pedersen et al., 2015). Additionally, rather small differences in particle size were found between the different alloys. We do not exclude the possibility that closer examination of the alloy microstructure might suggest a set of unit cell parameters that gives conforming predictions of ductility, but based on the current experimental data it is deemed unlikely to obtain a set of microstructural parameters that remedy the faulty predictions of the unit cell model under proportional loading.

From Figure 10d, we observe that the difference between simulations with and without a particle for the AlFe and AlMgSi alloys is rather small, whereas it is more prominent for the Al1.2Mn alloy. Since the average stress triaxiality for the Al1.2Mn alloy is the lowest obtained for all materials considered, this might indicate that the void nucleation process by particle decohesion is sensitive to the stress state, at least for stress triaxialities in the applied intermediate range. When the triaxiality is reduced, the resistance to matrix contraction imposed by the particle is greater, causing

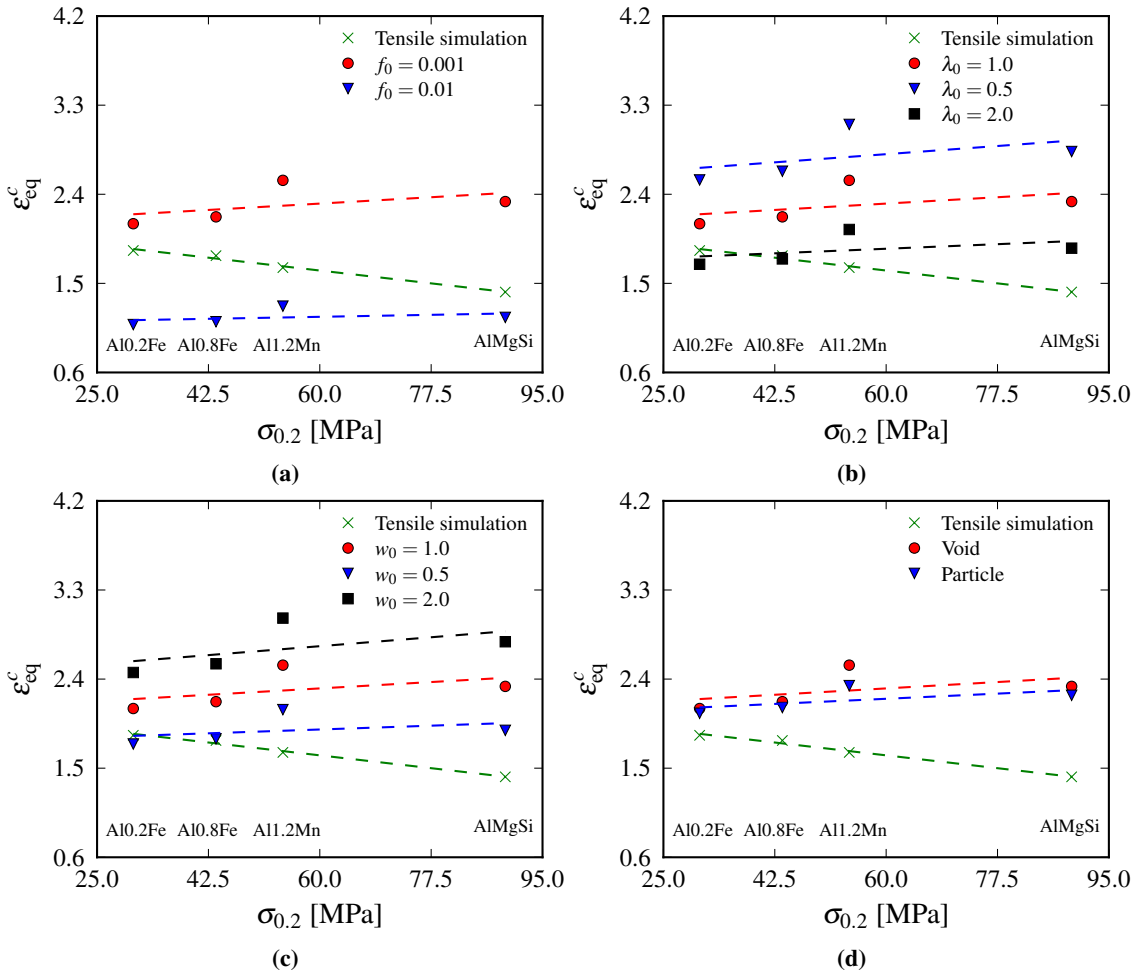

Figure 10: Failure strain curves from unit cell simulations using proportional loading paths compared with experimental failure strain data. Effects of (a) void size, (b) cell aspect ratio (void spacing), (c) void aspect ratio (void shape), and (d) void nucleation by particle decohesion. The reference unit cell contained a pre-existing void and was represented by $f_0 = 0.001$, $\lambda_0 = 1$, and $w_0 = 1$. Results for the reference cell are indicated by red lines and circle markers.

a larger discrepancy between simulations with and without a particle. Another possible explanation is that for the lowest stress triaxiality value, the matrix slides along the particle surface to a greater extent that for slightly larger stress triaxialities. This might lead to a violation of the adopted small-sliding contact formulation. Also, we must emphasize that the difference between unit cell predictions with and without a particle is highly dependent upon the nucleation criterion and cohesive surface parameters used in the simulations. A stronger cohesion would certainly yield greater difference in the predicted failure strains.

4.2.3. Non-proportional loading path

Based on the findings in the preceding section, it seems reasonable to assume that there are other mechanical sources of influence, potentially more decisive for ductility, on a microscopic level. In this regard, we find the recent investigations by Vadillo and Fernández-Sáez (2009), Zhang and Skallerud (2010), and Benzerga et al. (2012) particularly interesting. Since a change of loading path significantly alters the ductile fracture strain, it is expected that the continuously changing loading path exerted on a material element located in the middle section during necking plays a key role in the resulting ductility of the material.

A non-proportional loading path was prescribed to the unit cell. This was obtained by allowing the imposed

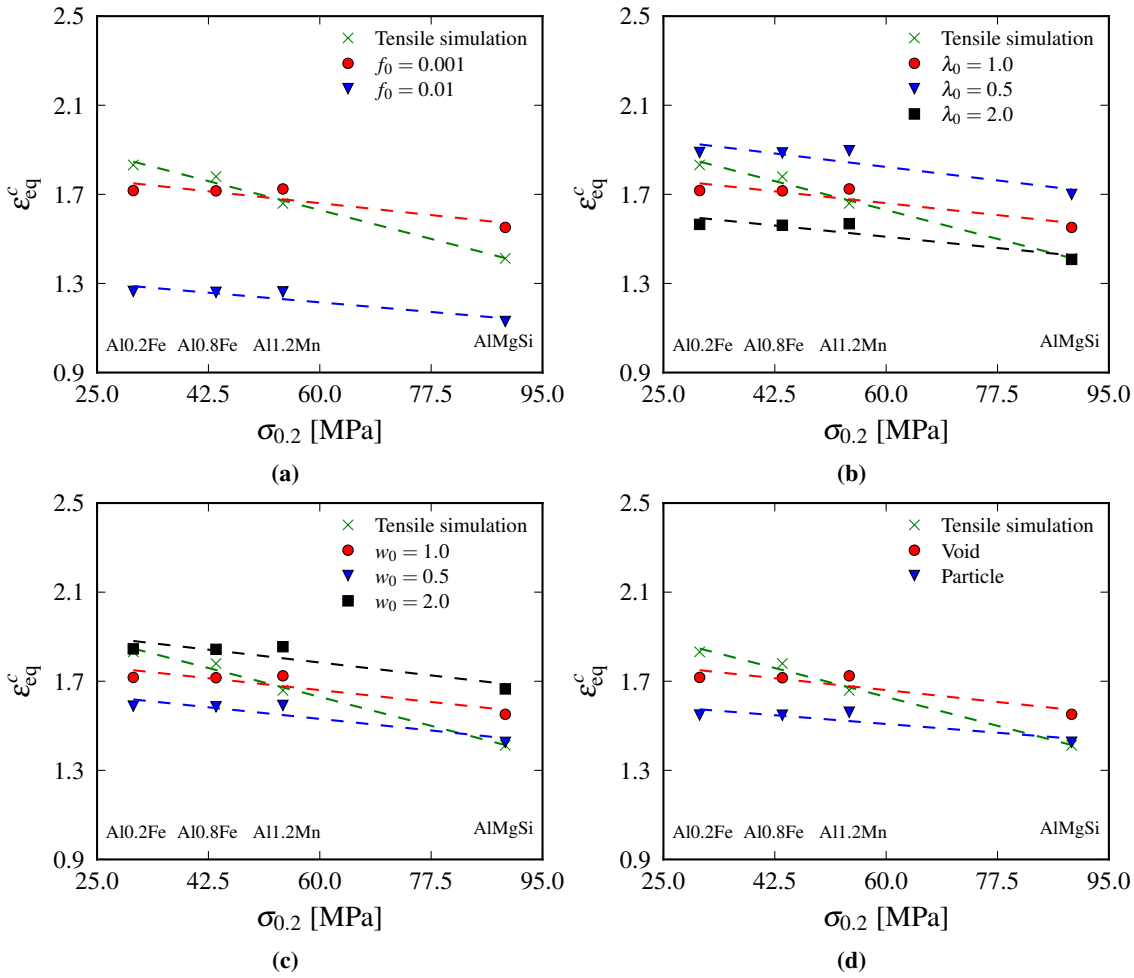

Figure 11: Failure strain curves from unit cell simulations using non-proportional loading path from tensile simulation. Effects of (a) void size, (b) cell aspect ratio (void spacing), (c) void aspect ratio (void shape), and (d) void nucleation by particle decohesion. The reference unit cell contained a pre-existing void and was represented by $f_0 = 0.001$, $\lambda_0 = 1$, and $w_0 = 1$. Results for the reference cell are indicated by red lines and circle markers.

macroscopic stress triaxiality to vary according to the polynomial given in Equation (12) using kinematic constraints defined through an MPC subroutine, as described in Section 3.2.1. The triaxiality polynomials for the different alloys are shown graphically in Figure 6b. Thus, the macroscopic loading applied to the unit cell boundaries was identical to that experienced by the critical element in the smooth tensile simulations under the assumption of the J_2 flow rule. This allows us to study the void evolution and underlying ductile fracture mechanism by void coalescence in detail for a realistic loading path, and investigate its influence on the predicted ductility of the different aluminium alloys. The reference cell geometry was modelled with a pre-existing void and microstructural parameters corresponding to $f_0 = 0.001$, $\lambda_0 = 1$ and $w_0 = 1$. A parameter study was performed, analogous to that undertaken with proportional loading in Section 4.2.2.

Results from unit cell simulations with non-proportional loading are plotted in Figure 11. Again, the failure strain in the experiments (Pedersen et al., 2015) are represented by the equivalent strain at material failure extracted from the critical element in the smooth tensile specimen simulations. A non-proportional loading path is seen to significantly influence coalescence strains and the associated failure strain curves. The slope of the failure strain curves are now, at least in an approximate sense, similar to the experimental data. From these results, we may also appreciate the fact that our reference model seems to be in good correspondence with the experimental data, as indicated by the red dashed

curves with circular markers in Figures 11a-11d.

Similar effects of varying the microstructural parameters as in Section 4.2.2 are also observed during non-proportional loading. The failure strain curves are effectively shifted up and down by changing the initial cell geometry. However, the difference between coalescence strain in simulations with and without particle for the Al1.2Mn alloy is now seen to be of the same order as for the other alloys. In general, the presence of a particle is seen to have greater effect on the unit cell predictions during non-proportional loading, by effectively reducing the coalescence strain values. This is ascribed to the resistance against matrix contraction when a particle is included, facilitating a more rapid coalescence process for the non-proportional loading paths when the stress triaxiality increases. However, we again remark that these results are sensitive to the adopted cohesive surface formulation.

An observation worth mentioning is that the coalescence strains for the AlFe and Al1.2Mn alloys are almost identical. This is in contradiction to the experimental data, where the AlFe alloys have comparable ductility while the Al1.2Mn alloy has lower ductility. This discrepancy is explained by the similar stress triaxiality evolution obtained in the critical element for these three alloys. However, their microstructure is taken to be similar in these analyses, which is not correct from a metallurgical point of view. This suggests that slightly different microstructure parameters, e.g. initial porosity f_0, should be used, which in turn could yield better correspondence with the experimental data.

A final conclusion may be drawn from these simulations. Changes in loading path during deformation have large impact on the predicted ductility, causing an earlier onset of void coalescence by internal necking of the intervoid ligament. These effects might be important to take into consideration, especially when unit cell simulations are used to generate fracture loci for given materials.

4.3. Smooth and notched tensile specimens with J_2 and GT material descriptions

Motivated by the findings from unit cell simulations with non-proportional loading, we find it interesting to assess the performance of the widely used GT model in terms of ductile fracture prediction capabilities. To this end, we performed simulations of smooth and notched tensile specimens similar to those used in Pedersen et al. (2015). Work-hardening of the matrix material was described by a two-term Voce rule with the material parameters found in Table 1. Comparisons are made with simulations using a J_2 flow theory material description with similar work-hardening parameters. In numerical simulations using the GT model to account for material softening, an initial porosity of $f_0 = 0.001$ was used to match the reference values from the unit cell study in Section 4.2.3. Material parameters $q_1 = 1.5$, $q_2 = 1.0$, and $q_3 = q_1^2$ were employed in all simulations, in accordance with the values initially proposed by Tvergaard (1982).

Figures 12a-12d show the true stress-logarithmic strain response for all four materials. Results from the numerical simulations of smooth and notched tensile specimens with notch radii $R = 2.0$ mm and $R = 0.8$ mm, using J_2 flow theory (dashed lines) and the GT model (dotted lines), are presented and compared with the experimental data (solid lines). The smooth tensile tests are well replicated by both material descriptions for all four alloys. This is expected, since data from the smooth tensile tests were used to calibrate the work-hardening model. However, results from the notched specimen simulations reveal that the true stress values calculated from the numerical analyses are larger than the corresponding values from the experiments. Greatest difference is obtained for the R0.8 notched specimens with J_2 flow theory. In the case of the Al0.8Fe alloy, the true stress at material failure in the FE simulation is about 15% higher than the tensile test. The Al0.2Fe and Al1.2Mn alloys both have a maximum difference in true stress of about 10% at material failure, whereas the AlMgSi alloy yields practically conforming stress-strain curves in simulations and experiments. The over-estimation of the stress level in simulations of notched tensile specimens has been discussed in previous studies and may be attributed to a possible pressure dependency of plastic yielding (see e.g. Spitzig and Richmond (1984); Wilson (2002); Bai and Wierzbicki (2008)), a dependence of the third invariant of the stress deviator J_3 (see e.g. Bai and Wierzbicki (2008)), or plastic anisotropy effects (see e.g. Fourmeau et al. (2011)) related to the imposed notch constraint. In this regard, using the GT porous plasticity model to account for material softening causes minor improvements on the predicted stress-strain curves. This indicates that the void induced pressure dependency of the GT model is not sufficient to correct the predicted response of the notched tensile specimens. Since the stress state is assumed to be axisymmetric, corresponding to a constant Lode parameter, any effects of a potential J_3 dependence are not captured. This was also verified by running notched specimen simulations with a high-exponent Hershey yield function. These simulations gave similar response as the adopted J_2 flow theory, but the results are not presented in this paper for the sake of brevity. Thus, we believe that the observed discrepancies are most likely due to weak plastic

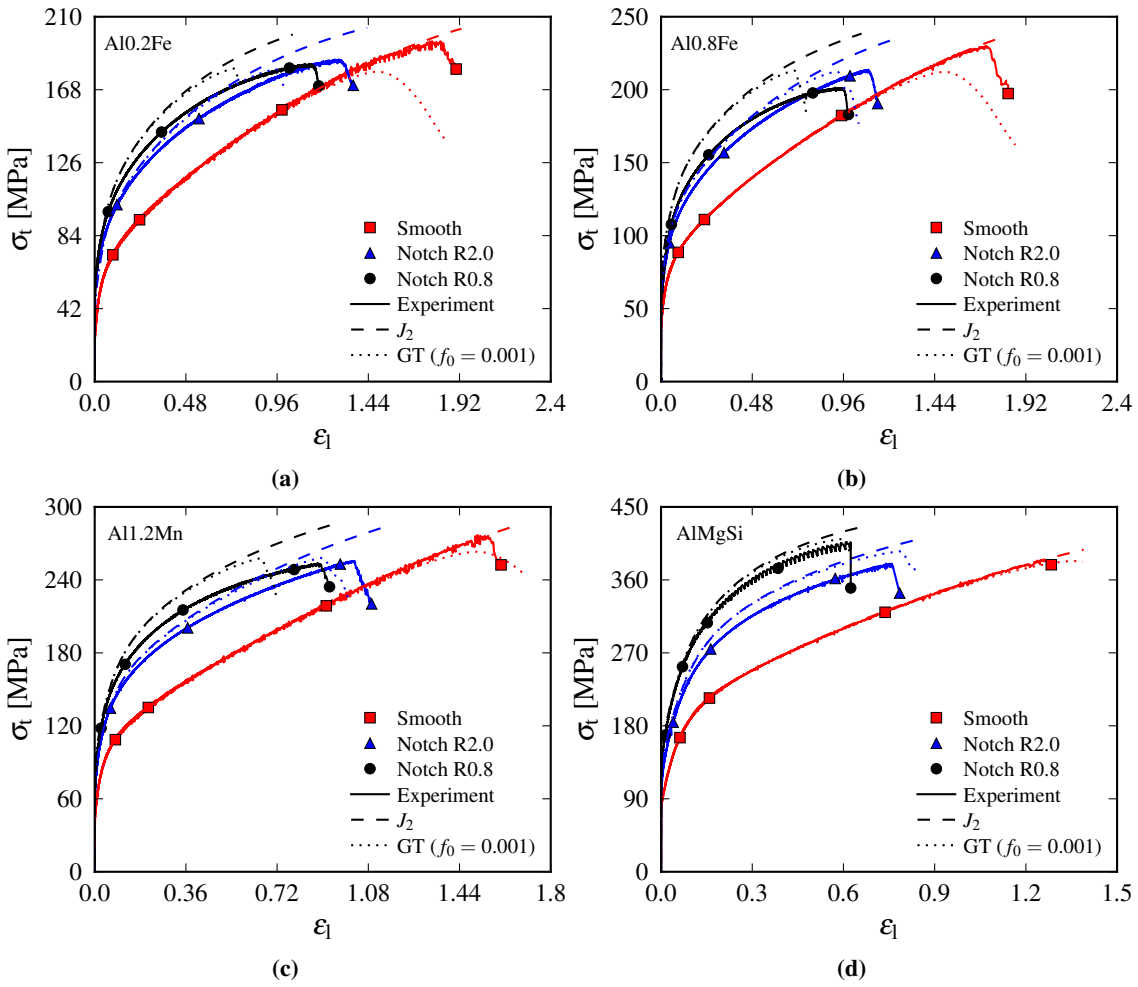

Figure 12: True stress-logarithmic strain curves evaluated from diameter reduction. Solid lines correspond to the experimental data, dashed lines to simulations with the J_2 flow theory, and dotted lines to simulations with the GT yield function. Each subfigure shows plots for smooth, R2.0 and R0.8 notched specimens. The materials are (a) Al0.2Fe, (b) Al0.8Fe, (c) Al1.2Mn, and (d) AlMgSi. All simulations with the GT model were carried out using an initial porosity of $f_0 = 0.001$.

anisotropy. The r-values shown in Figure 1b indicate moderate anisotropic behaviour for the AlFe alloys. This could explain, at least for these two alloys, the deviation in the notched stress-strain curves.

The GT model improves the predicted material response in the vicinity of material failure for all materials. In the case of smooth tensile specimens, the onset of material softening is seen to be well captured by the GT model for the Al1.2Mn and AlMgSi alloys, while conservative estimates are obtained for both AlFe alloys. For the notched specimens, conservative estimates of material failure are obtained for the AlFe and Al1.2Mn alloys, while slightly non-conservative estimates are obtained for the AlMgSi alloy.

Since the loading paths applied to the unit cell were found from simulations of smooth tensile specimens using the J_2 flow theory, it is interesting to see how the stress triaxiality evolves in corresponding numerical analyses using the GT model. Figure 13 shows the evolution of stress triaxiality in unit cell simulations with non-proportional loading and from the critical element of the smooth tensile specimens using both J_2 and GT material descriptions. The porosity evolution of the critical element in the GT simulations, i.e. void growth, is also presented. All curves are plotted up to the point of material failure, thus up to equivalent strain values of ε_{eq}^{c} from the respective analyses. Figures 13a-13d clearly indicate that the loading paths observed by a material element in the middle section of the smooth tensile specimen are similar up to large values of equivalent strain. However, in the proximity of material failure the

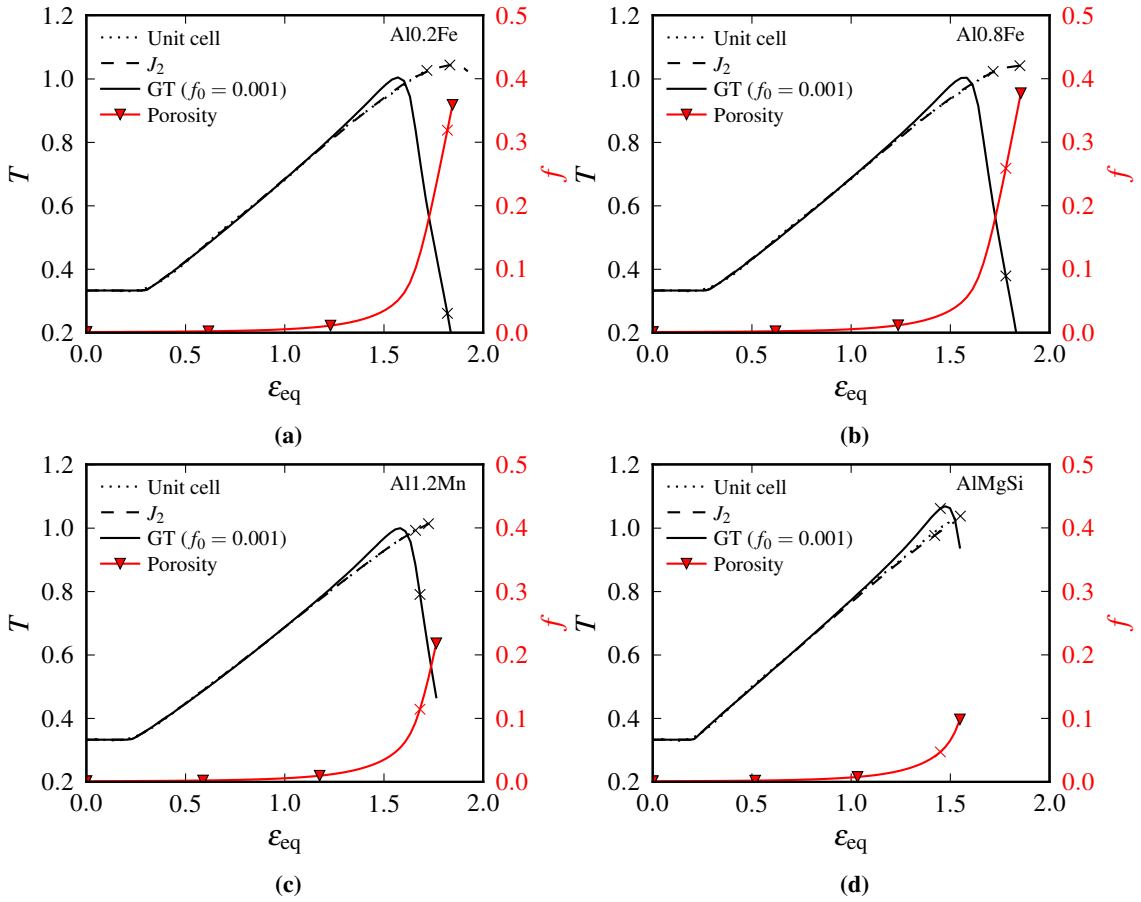

Figure 13: Comparison of stress triaxiality evolution (left ordinate axis T) from unit cell simulations (dotted line) and smooth tensile specimen simulations using both J_2 (dashed line) and GT (solid line) yield functions. In simulations with the GT model, the initial porosity was $f_0 = 0.001$ for all four materials. The porosity evolution (right ordinate axis f) in the GT simulations is also plotted. Data points up to material failure are included.

stress triaxiality first increases slightly, then decreases abruptly when the GT model is used, except for the AlMgSi alloy. This is directly related to the fact that the AlMgSi alloy is the only material yielding a non-conservative global response. Thus, if these loading paths were prescribed to the unit cell instead of those from the J_2 analyses, the onset of void coalescence might be altered, yielding different coalescence strain values. This indicates that there are some ambiguities associated with the extraction of local field quantities from numerical simulations, even when the global response coincides. We note that the curves for the J_2 material and the unit cell are seen to coincide, which means that the boundary conditions of the unit cell were properly prescribed. We believe the explanation for the observed drop in stress triaxiality is related to a local bifurcation within the critical element. The two integration points closest to the middle section of the specimen are more constrained than the outer two, making them more favourable for void growth and plastic volumetric deformation. In turn, a localization occurs within the element, relieving the outer two integration points from hydrostatic stress, while softening occurs very rapidly in the two heavily constrained integration points. This causes the stress triaxiality to decrease on average within the element.

4.4. Calibration process based on initial porosity

The last part of this study aims at presenting a possible calibration process using a combination of micromechanical analyses and tensile simulations. It is noted that material data for the work-hardening must be obtained in advance. Again, polynomials fitted to the evolution of stress triaxiality with equivalent strain (see Section 3.1) from the smooth

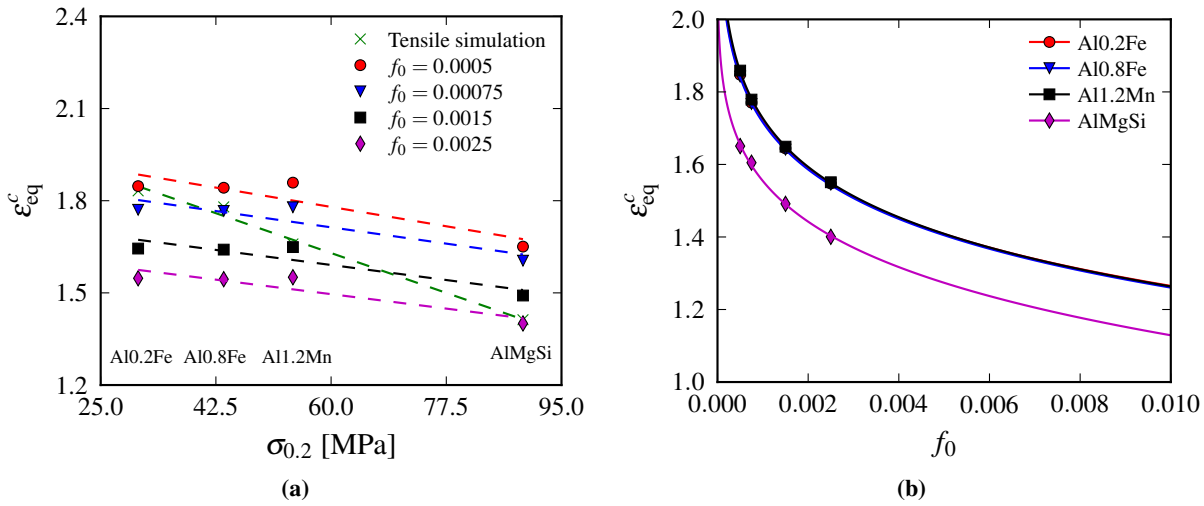

Figure 14: Coalescence strain values obtained by changing initial porosity f_0 in order to conform with the experimental data. The results shown are (a) coalescence strain against 0.2% proof stress, and (b) coalescence strain against initial porosity.

Table 4: Constants obtained from a curve fit of numerical results for coalescence strain at different initial porosity levels to a power law function, as given by Equation (31). The last row shows values of initial void volume fraction f_0 from unit cell simulations that conforms with coalescence strain values determined from the experimental data.

Material	A	B	C	f_0
Al0.2Fe	-4.876	0.0557	5.037	0.0005
Al0.8Fe	-4.419	0.0651	4.535	0.00075
Al1.2Mn	-5.420	0.0493	5.582	0.0015
AlMgSi	-2.888	0.1580	2.524	0.0025

tensile simulations are used as input in the unit cell analyses, similar to the procedure in Section 4.2.3. A parameter study on the initial porosity (f_0) is carried out such that the coalescence strain values obtained from the unit cell simulations match the corresponding equivalent strain values from the smooth tensile specimens given in Table 2.

A number of f_0-values are applied to the unit cell in the search for initial porosities yielding similar coalescence strains as those obtained from the smooth tensile specimen simulations. Note that this gives different f_0-values for the different alloys. The resulting initial porosities are given in Table 4. Linear failure strain curves and corresponding coalescence strain values from the parameter study are shown in Figure 14a. Each of these curves yields conforming coalescence strain for one of the materials.

In the process of finding appropriate values of f_0 for the different alloys, it might be interesting to determine an empirical relation between coalescence strain and initial porosity for the different materials. To this end, we assume that the relation may be described using a power law on the form

$$\varepsilon^c_{eq} = A f_0^B + C \tag{31}$$

where A, B, and C are constants that need to be found by an appropriate curve fitting procedure. For this purpose, we used a least-square approach. The resulting functions and numerical data are plotted in Figure 14b and the calibrated constants are given in Table 4. The main observation is that the empirical relations are similar for the AlFe and Al1.2Mn alloys, which is caused by their comparable ductility in unit cell simulations.

In the last part of this study, we used the initial porosities given in Table 4 in simulations of smooth and notched tensile specimens with the GT model. The true stress-logarithmic strain curves are shown in Figure 15, where the experimental data and results from simulations with initial porosities of $f_0 = 0.001$ are plotted for comparison. Results

from the different tensile simulations are in general enhanced using the calibrated porosity values. Moreover, all simulations yield conservative predictions of material failure, which is important in structural design. However, predictions for the Al1.2Mn alloy and the R0.8 notched AlMgSi specimen are impaired. Also, the over-estimated true stress values are not remedied by using the calibrated f_0-values. This implies that a simple calibration process, purely based on changing the initial porosity of the material, is not sufficient to accurately predict the material behaviour in terms of tensile stress-strain response. Certainly, if even feasible, this would require to use a very large initial porosity with the undesired effect of impairing the ductility predictions of the plasticity model. This indicates that the GT model is not sufficiently refined to capture all aspects of the ductile failure process properly, since fair predictions of one response parameter comes at the expense of weak predictions of another response parameter. Other models are proposed in the literature that might enhance the results both in terms of stress-strain response and ductility predictions (see e.g. Benzerga and Leblond (2010)).

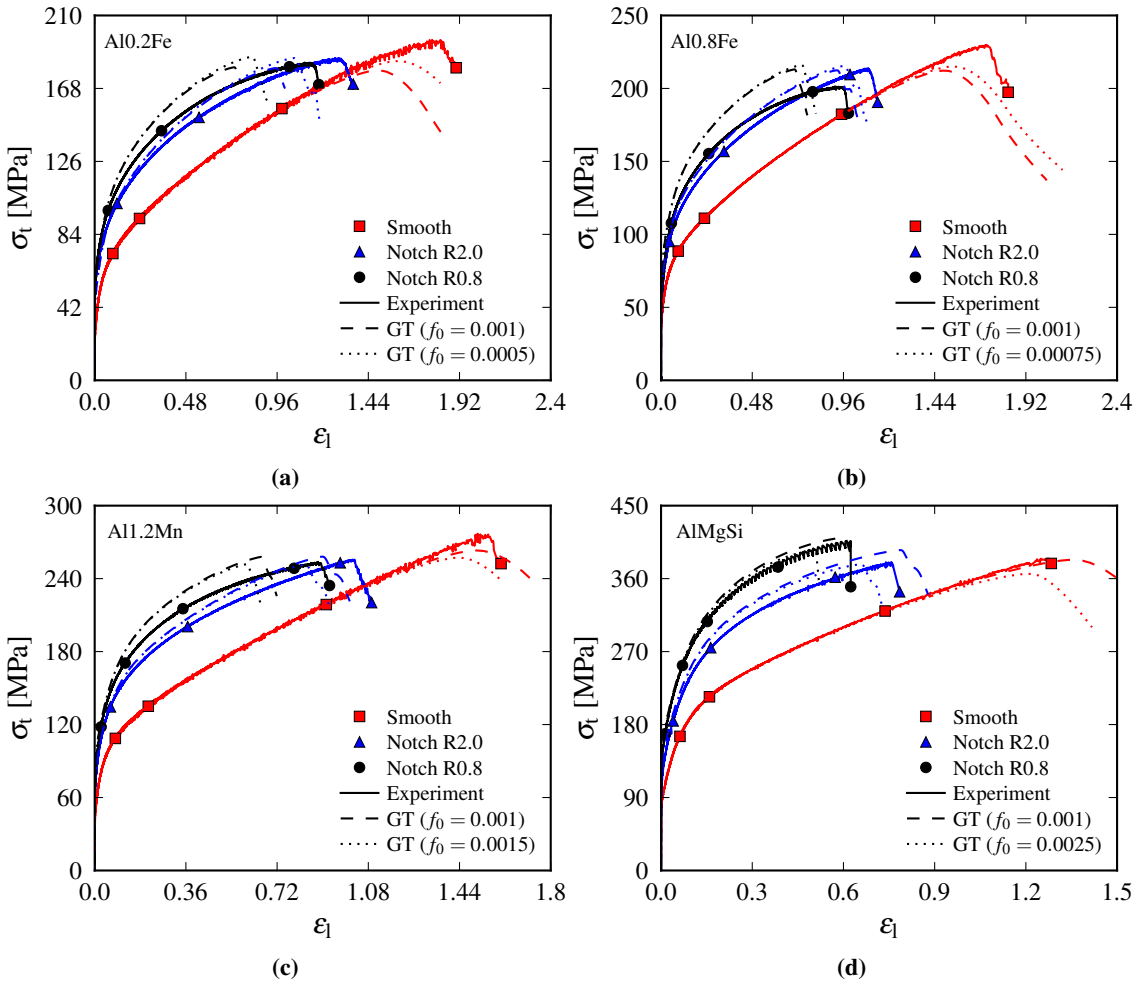

Figure 15: True stress-logarithmic strain curves evaluated from tensile tests and numerical simulations. Solid lines correspond to experimental data, dashed lines to simulations with the GT model and constant initial porosity of $f_0 = 0.001$, and dotted lines to simulations with the GT model and the calibrated f_0-values found in Table 4. Each subfigure shows plots for smooth, R2.0 and R0.8 notched specimens. The materials are (a) Al0.2Fe, (b) Al0.8Fe, (c) Al1.2Mn, and (d) AlMgSi.

Although much focus has been directed towards the deficiencies of the GT model in the numerical simulations carried out in this study, we should also take care to note that the GT model greatly enhances numerical predictions as compared with the J_2 flow theory. The material softening is, broadly speaking, quite well captured by the GT model for all four aluminium alloys with the true stress decreasing rapidly as the plastic flow localizes in the necking region. In

addition, the logarithmic strain at material failure is in fair agreement with values extracted from experiments, yielding good predictions of the material ductility.

We lastly mention that efforts could be made towards calibrating the microstructural parameters of the GT model (q_i) to yield better correspondence with unit cell simulations. A number of previous papers have dealt with such calibration processes. Notable contributions are studies by Faleskog et al. (1998) and Kim et al. (2004). Also, in a recent study by Bomarito and Warner (2015) non-homogeneous loading paths are taken into account when homogenizing micromechanical simulation results using a Gurson constitutive model. This was done by allowing q_1 and q_2 to be functions of the stress triaxiality and Lode parameters. However, these types of calibrations seem highly problem dependent, and might yield inaccurate predictions when applied to other arbitrary deformation paths that often emerge in structural problems. Also, such procedures do not necessarily guarantee the convexity of the yield surface.

5. Concluding remarks

Results from unit cell simulations carried out in the present study demonstrate that non-proportional loading greatly influences ductility. This implies that fracture loci obtained by keeping the loading state proportional are most likely unable to yield accurate predictions of ductile failure, unless the deformations imposed to a material body causes a nearly proportional loading state. This is rarely the case in structural applications. Also, the demonstrated loading path dependence makes it more difficult to generate specific fracture loci, since an infinite number of loading paths can be assigned to obtain the same average stress state. Each of these loading paths would probably yield a unique fracture locus.

Numerical simulations of smooth tensile specimens were in good correspondence with experiments for both the J_2 flow theory and the GT model, where the latter model also yielded fair predictions of the ductility. However, we were not able to obtain an accurate true stress-logarithmic strain response with neither the J_2 yield function nor the GT model in numerical simulations of the notched tensile specimens, presumably due to weak plastic anisotropy. In the case of the GT model, the overall predictions of material softening and ductility were in general acceptable. The proposed calibration process, based on a parameter study using the initial porosity, did not remedy the deficiencies observed in the global response of the notched tensile specimens. However, the overall predictions for all materials were enhanced, and conservative predictions of failure were obtained for all tensile specimens used in this study. This suggests that a more refined material model, taking several microstructural parameters into account, should be used.

It is realized that the experimental failure strain for the different aluminium alloys also could have been replicated by changing other microstructural parameters. As seen from the figures presented in Section 4.2, all four parameters investigated in this study can be changed such that coalescence strains conform with the experimental data. However, in the porous plasticity model used in this paper, only the void volume fraction is accounted for. Thus, it was natural to use this microstructural parameter in a preliminary attempt to model the ductile fracture process on a global scale.

Acknowledgements

The financial support of this work from the Structural Impact Laboratory (SIMLab), Centre for Research-based Innovation (CRI) at the Norwegian University of Science and Technology (NTNU), is gratefully acknowledged.

References

Abaqus, 2013. Version 6.13. Dassault Systèmes Simulia Corp., Providence, RI, USA.

Achani, D., Hopperstad, O. S., Lademo, O. G., 2009. Behaviour of extruded aluminium alloys under proportional and non-proportional strain paths. Journal of Materials Processing Technology 209, 4750–4764.

Bai, Y., Wierzbicki, T., 2008. A new model of metal plasticity and fracture with pressure and Lode dependence. International Journal of Plasticity 24, 1071–1096.

Bao, Y., Wierzbicki, T., 2004. On fracture locus in the equivalent strain and stress triaxiality space. International Journal of Mechanical Sciences 46, 81–98.

Barsoum, I., Faleskog, J., 2007a. Rupture mechanisms in combined tension and shear-Experiments. International Journal of Solids and Structures 44, 1768–1786.

Barsoum, I., Faleskog, J., 2007b. Rupture mechanisms in combined tension and shear-Micromechanics. International Journal of Solids and Structures 44, 5481–5498.

Barsoum, I., Faleskog, J., 2011. Micromechanical analysis on the influence of the Lode parameter on void growth and coalescence. International Journal of Solids and Structures 48, 925–938.
Basu, S., Benzerga, A. A., 2015. On the path-dependence of the fracture locus in ductile materials: Experiments. International Journal of Solids and Structures 71, 79–90.
Becker, R., Smelser, R. E., Richmond, O., Appleby, E. J., 1989. The effect of void shape on void growth and ductility in axisymmetric tension tests. Metallurgical Transactions A 20A, 853–861.
Benzerga, A. A., Leblond, J. B., 2010. Ductile Fracture by Void Growth to Coalescence. Advances in Applied Mechanics 44, 169 —- 305.
Benzerga, A. A., Leblond, J.-b., 2014. Effective Yield Criterion Accounting for Microvoid Coalescence. Journal of Applied Mechanics 81, 1–7.
Benzerga, A. A., Surovik, D., Keralavarma, S. M., 2012. On the path-dependence of the fracture locus in ductile materials - Analysis. International Journal of Plasticity 37, 157–170.
Bomarito, G., Warner, D., 2015. Micromechanical investigation of ductile failure in Al 5083-H116 via 3D unit cell modeling. Journal of the Mechanics and Physics of Solids 74, 97–110.
Bonfoh, N., Lipinski, P., 2007. Ductile damage micromodeling by particles' debonding in metal matrix composites. International Journal of Mechanical Sciences 49, 151–160.
Brocks, W., Sun, D.-Z., Hönig, A., 1995. Verification of the transferability of micromechanical parameters by cell model calculations with visco-plastic materials. International Journal of Plasticity 11, 971–989.
Brocks, W., Sun, D.-Z., Hönig, A., 1996. Verification of micromechanical models for ductile fracture by cell model calculations. Computational Materials Science 7, 235–241.
Chandra, N., Li, H., Shet, C., Ghonem, H., 2002. Some issues in the application of cohesive zone models for metal-ceramic interfaces. International Journal of Solids and Structures 39, 2827–2855.
Chow, C. L., Yu, L. G., Tai, W. H., Demeri, M. Y., 2001. Prediction of forming limit diagrams for AL6111-T4 under non-proportional loading. International Journal of Mechanical Sciences 43, 471–486.
Cockcroft, M., Latham, D., 1968. Ductility and the workability of Metals. Journal of the Institute of Metals 96, 33–39.
Dunand, M., Mohr, D., 2011. Optimized butterfly specimen for the fracture testing of sheet materials under combined normal and shear loading. Engineering Fracture Mechanics 78, 2919–2934.
Dunand, M., Mohr, D., 2014. Effect of Lode parameter on plastic flow localization after proportional loading at low stress triaxialities. Journal of the Mechanics and Physics of Solids 66 (1), 133–153.
Eikrem, P. A., Zhang, Z. L., Østby, E., Nyhus, B., 2008. Numerical study on the effect of prestrain history on ductile fracture resistance by using the complete Gurson model. Engineering Fracture Mechanics 75, 4568–4582.
Faleskog, J., Barsoum, I., 2013. Tension-torsion fracture experiments - Part I: Experiments and a procedure to evaluate the equivalent plastic strain. International Journal of Solids and Structures 50, 4241–4257.
Faleskog, J., Gao, X., Shih, C. F., 1998. Cell model for nonlinear fracture analysis – I. Micromechanics calibration. International Journal of Fracture 89 (4), 355–373.
Ferrante, J., Smith, J. R., 1985. Theory of the bimetallic interface. Physical Review B 31, 3427–3434.
Fourmeau, M., Børvik, T., Benallal, A., Lademo, O. G., Hopperstad, O. S., 2011. On the plastic anisotropy of an aluminium alloy and its influence on constrained multiaxial flow. International Journal of Plasticity 27, 2005–2025.
Gao, X., Kim, J., 2006. Modeling of ductile fracture: Significance of void coalescence. International Journal of Solids and Structures 43, 6277–6293.
Gao, X., Zhang, G., Roe, C., 2010. A Study on the Effect of the Stress State on Ductile Fracture. International Journal of Damage Mechanics 19 (1), 75–94.
Gao, X., Zhang, T., Hayden, M., Roe, C., 2009. Effects of the stress state on plasticity and ductile failure of an aluminum 5083 alloy. International Journal of Plasticity 25, 2366–2382.
Gao, X., Zhang, T., Zhou, J., Graham, S. M., Hayden, M., Roe, C., 2011. On stress-state dependent plasticity modeling: Significance of the hydrostatic stress, the third invariant of stress deviator and the non-associated flow rule. International Journal of Plasticity 27, 217–231.
Gurson, A. L., 1977. Continuum Theory of Ductile Rupture by Void Nucelation and Growth: Part I – Yield Criteria and Flow Rules for Porous Ductile Media. Journal of Engineering Materials and Technology 99 (1), 2—-15.
Haltom, S. S., Kyriakides, S., Ravi-Chandar, K., 2013. Ductile failure under combined shear and tension. International Journal of Solids and Structures 50, 1507–1522.
Hannard, F., Pardoen, T., Maire, E., Bourlot, C. L., Mokso, R., Simar, A., 2016. Characterization and micromechanical modelling of microstructural heterogeneity effects on ductile fracture of 6xxx aluminium alloys. Acta Materialia 103, 558–572.
Hill, R., 1967. The essential structure of constitutive laws for metal composites and polycrystals. Journal of the Mechanics and Physics of Solids 15, 79–95.
Johnson, G. R., Cook, W. a., 1985. Fracture characteristic of three metals subjected to various strains, strain rates, temperatures and pressures. Engineering Fracture Mechanics 21, 31–48.
Khan, A. S., 1990. An experimental study of large finite plastic deformation in annealed 1100 aluminum during proportional and nonproportional biaxial compression. International Journal of Plasticity 6, 485–504.
Kim, J., Gao, X., Srivatsan, T. S., 2004. Modeling of void growth in ductile solids: Effects of stress triaxiality and initial porosity. Engineering Fracture Mechanics 71, 379–400.
Koplik, J., Needleman, A., 1988. Void growth and coalescence in porous plastic solids. International Journal of Solids and Structures 24 (8), 835–853.
Lin, R. C., Steglich, D., Brocks, W., Betten, J., 2006. Performing RVE calculations under constant stress triaxiality for monotonous and cyclic loading. International Journal for Numerical Methods in Engineering 66, 1331–1360.
Liu, G., Scudino, S., Li, R., Kühn, U., Sun, J., Eckert, J., 2011. Coupling effect of primary voids and secondary voids on the ductile fracture of heat-treatable aluminum alloys. Mechanics of Materials 43, 556–566.
Lloyd, D. J., 2003. The scaling of the tensile ductile fracture strain with yield strength in Al alloys. Scripta Materialia 48, 341–344.
Maire, E., Zhou, S., Adrien, J., Dimichiel, M., 2011. Damage quantification in aluminium alloys using in situ tensile tests in X-ray tomography. Engineering Fracture Mechanics 78, 2679–2690.

Marcadet, S. J., Mohr, D., 2015. Effect of Compression-tension Loading Reversal on the Strain to Fracture of Dual Phase Steel Sheets. International Journal of Plasticity 72, 21–43.
Marini, B., Mudry, F., Pineau, A., 1985. Ductile rupture of A508 steel under nonradial loading. Engineering Fracture Mechanics 22, 375–386.
McVeigh, C., Vernerey, F., Liu, W. K., Moran, B., Olson, G., 2007. An interactive micro-void shear localization mechanism in high strength steels. Journal of the Mechanics and Physics of Solids 55 (2), 225–244.
Needleman, A., 1972. Void Growth in an Elastic-Plastic Medium. Journal of Applied Mechanics 39, 964–970.
Papasidero, J., Doquet, V., Mohr, D., 2015. Ductile fracture of aluminum 2024-T351 under proportional and non-proportional multi-axial loading: BaoWierzbicki results revisited. International Journal of Solids and Structures 69-70, 459–474.
Pardoen, T., 2006. Numerical simulation of low stress triaxiality ductile fracture. Computers & Structures 84, 1641–1650.
Pedersen, K. O., Westermann, I., Furu, T., Børvik, T., Hopperstad, O. S., 2015. Influence of microstructure on work-hardening and ductile fracture of aluminium alloys. Materials & Design 70, 31–44.
Reyes, A., Hopperstad, O. S., Berstad, T., Lademo, O. G., 2008. Prediction of necking for two aluminum alloys under non-proportional loading by using an FE-based approach. International Journal of Material Forming 1, 211–232.
Rose, J. H., Ferrante, J., Smith, J. R., 1981. Universal binding energy curves for metals and bimetallic interfaces. Physical Review Letters 47, 675–678.
Rose, J. H., Smith, J. R., Ferrante, J., 1983. Universal features of bonding in metals. Physical Review B 28, 1835–1845.
Roth, C. C., Mohr, D., 2015. Ductile Fracture Experiments with Locally Proportional Loading Histories. International Journal of Plasticity 79, 328–354.
Segurado, J., Llorca, J., 2005. A computational micromechanics study of the effect of interface decohesion on the mechanical behavior of composites. Acta Materialia 53, 4931–4942.
Søvik, O. P., Thaulow, C., 1997. Growth of spheroidal voids in elastic-plastic solids. Fatigue & Fracture of Engineering Materials & Structures 20, 1731–1744.
Spitzig, W. A., Richmond, O., 1984. The effect of pressure on the flow stress of metals. Acta Metallurgica 32, 457—-463.
Steglich, D., Brocks, W., 1997. Micromechanical modelling of the behaviour of ductile materials including particles. Computational Materials Science 9, 7–17.
Steglich, D., Brocks, W., Heerens, J., Pardoen, T., 2008. Anisotropic ductile fracture of Al 2024 alloys. Engineering Fracture Mechanics 75, 3692–3706.
Suh, Y. S., Joshi, S. P., Ramesh, K. T., 2009. An enhanced continuum model for size-dependent strengthening and failure of particle-reinforced composites. Acta Materialia 57, 5848–5861.
Tekoğlu, C., Hutchinson, J. W., Pardoen, T., 2015. On localization and void coalescence as a precursor to ductile fracture. Philosophical Transactions of the Royal Society of London A: Mathematical, Physical and Engineering Sciences 373, 1 – 19.
Toda, H., Oogo, H., Horikawa, K., Uesugi, K., Takeuchi, A., Suzuki, Y., Nakazawa, M., Aoki, Y., Kobayashi, M., 2014. The True Origin of Ductile Fracture in Aluminum Alloys. Metallurgical and Materials Transactions A 45A, 765–776.
Tvergaard, V., 1981. Influence of voids on shear band instabilities under plane strain conditions. International Journal of Fracture 17 (4), 389–407.
Tvergaard, V., 1982. On localization in ductile materials containing spherical voids. International Journal of Fracture 18, 237–252.
Vadillo, G., Fernández-Sáez, J., 2009. An analysis of Gurson model with parameters dependent on triaxiality based on unitary cells. European Journal of Mechanics - A/Solids 28, 417–427.
Westermann, I., Pedersen, K. O., Furu, T., Børvik, T., Hopperstad, O. S., 2014. Effects of particles and solutes on strength, work-hardening and ductile fracture of aluminium alloys. Mechanics of Materials 79, 58–72.
Williams, J. J., Segurado, J., LLorca, J., Chawla, N., 2012. Three dimensional (3D) microstructure-based modeling of interfacial decohesion in particle reinforced metal matrix composites. Materials Science and Engineering A 557, 113–118.
Wilson, C. D., 2002. A Critical Reexamination of Classical Metal Plasticity. Journal of Applied Mechanics 69, 63–68.
Xu, X.-P., Needleman, A., 1993. Void nucleation by inclusion debonding in a crystal matrix. Modelling and Simulation in Materials Science and Engineering 1, 111–132.
Yu, H., Olsen, J. S., He, J., Zhang, Z., 2016. Effects of loading path on the fracture loci in a 3D space. Engineering Fracture Mechanics 151, 22–36.
Zhang, Z., Skallerud, B., 2010. Void Coalescence With and Without Prestrain History. International Journal of Damage Mechanics 19, 153–174.